Part III.

Interdepartmental research activities – selected highlights

Interplay of hydrogen embrittlement and solute-defect interactions in steels

G. Hachet[1], A. Tehranchi[2], T. Hickel[2], B. Gault[1], D. Ponge[1], J. Neugebauer[2], D. Raabe[1], M. J. Duarte[3], J. Rao[3], M. Rohwerder[4], G. Dehm[3]

[1]MA, [2]CM, [3]SN, [4]GO

Steel is one of the most promising candidates for storing and transporting hydrogen because of its flexibility in forming different microstructures. High-strength steels are expected to be widely used, but are impacted by hydrogen embrittlement (HE). Here, we describe two parallel projects concerned with advancing the understanding of HE by combining advanced experiments and modeling and offering alternative materials design routes to enhance resistance against HE.

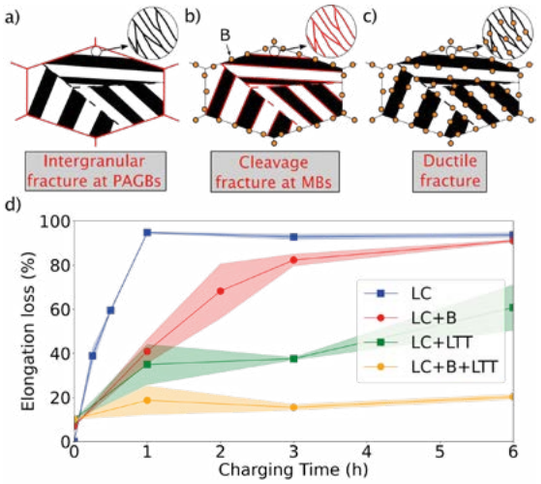

Fig. 1: *Concept of the project and first results.* ***a.*** *Intergranular fracture of H-charged LC steel.* ***b.*** *Intergranular fracture of H-charged LC+B steel.* ***c.*** *Ductile fracture of H-charged tempered (X+LTT) steel. Boron protects all boundaries.* ***d.*** *Elongation loss of LC, LC+B, LC+LTT and LC+B+LTT.*

The first focus is on low-carbon (LC) martensite, a metastable microstructure formed by fast quenching of austenite to room temperature. LC's microstructure contains a hierarchical substructure (Fig. 1) with boundaries formed before quenching, called prior austenite grain boundaries (PAGBs), and after quenching, called martensite boundaries (MBs). In H-containing environments, steel observes an elongation loss, defined as the ratio of (i) the reduction of the total elongation of a system due to H and (ii) the total elongation of the system without H. This elongation loss is observed in steels because PAGBs are the weakest microstructural features, causing a transition from ductile to intergranular, brittle fracture (Figs. 1 a, d).

Boron microalloying such steels (LC+B) is known to lead to B segregation to PAGBs, and not to MBs. With B addition, the damage mechanism due to H shifts to cleavage fracture localized at MBs (Figs. 1.b, d) [1]. Low-temperature tempering (LTT) at 160°C for 4 h is conducted to protect the MBs from HE. This heat treatment aims to activate the mobility of the remaining B and C in solid solution to segregate them into MBs (Figs 1.c, d). It improves the resistance against HE of the steel, even without the addition of B. However, the best results are observed when combining B doping and LTT (LC+B+LTT), showing a synergic effect of the solute and the treatment.

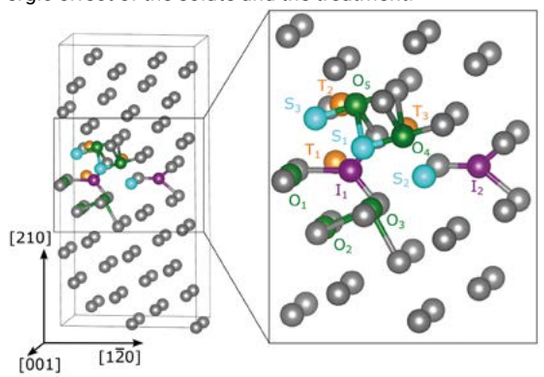

Fig. 2: *(a) Geometry of the supercell containing bcc FeΣ5 (210) symmetric tilt GB. (b) The binding sites at GB. Letters O, T, and I denote octahedral, tetrahedral, and interstitial sites, respectively.*

Ab initio calculations have been performed to shed light on the fundamental mechanism responsible for the improved HE resistance. The segregation of B and H to bcc FeΣ5 (210) symmetric tilt grain boundary (GB) is depicted in Fig. 2. Both solutes strongly segregate in sites I1 and I2. However, when B is already segregating to site I1, the interaction between H and the B-doped GB becomes repulsive. It prevents the H segregation and the intergranular fracture, besides increasing the cohesion of the GB [1].

A second focus is on assessing the effect of diffusible hydrogen on the mechanical behaviour. This is extremely relevant to understand the complex interactions of hydrogen in steels. Binary alloys are used here to understand and model the body-centered structure of ferritic steels, with an emphasis on Fe-Cr as Cr is commonly used to provide resistance against corrosion and oxidation in steels. By combining a multidisciplinary approach, each microstructural feature (bulk structure, grain boundaries, interfaces, precipitates…) is analysed independently to evaluate specific embrittlement mechanisms caused by its interaction with hydrogen, define dominant mechanisms, and provide guidelines for alloy design.

Our methodology uses the unique instrumentation developed at MPI-SusMat for nanoindentation testing during hydrogen loading [2]. Applied to a single crystal with low dislocation density, it shows a linear increase in hardness with increased hydrogen content, until reaching a quasi-equilibrium state [3]. This hardening effect can be explained by the interaction of hydrogen with dislocations and its accumulation forming clusters that limit their movement. These particular analyses were conducted on binary Fe alloys with Cr, Al, or Ni as substitutional elements. Cr content was also varied from 8 to 20 wt.%, to cover the range of Cr in ferritic steels.

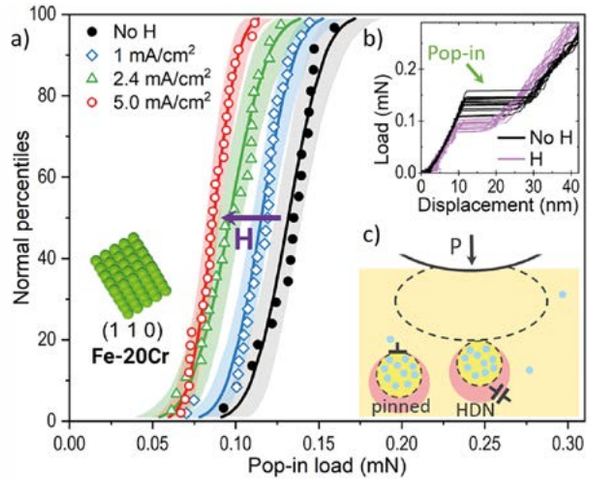

Fig. 4: *(a) Probability plots of pop-in load before and during hydrogen charging at different applied potentials (an increase in the current density indicates an increase in the hydrogen content). (b) Close-up of the nanoindentation load vs. displacement curves showing a decrease in the pop-in load due to hydrogen loading. (c) Schematic of nanohydrides formation during nanoindentation.*

The diffusion behaviour was analysed by Kelvin probe measurements, as in the example of Fig. 3a. While the increase in solute atoms (Cr, Al, Ni) decreases the hydrogen diffusivity in the alloy, it also increases the solubility of hydrogen, acting as flat trapping sites. A similar behaviour is observed when increasing the initial alloy's dislocation density. In a further step, it is shown that the backside hydrogen charging during nanoindentation [2] is a reliable technique for analyzing time-dependent and dynamic changes in the mechanical behaviour occurring during hydrogen absorption and release. The hardness evolution in the initial hydrogen loading segment (black dots in Fig. 3b) was simulated based on a non-steady state model to calculate the diffusion coefficient of hydrogen in Fe-Cr alloys (red line in Fig. 3b). The diffusion coefficient obtained using the changes in hardness as diffusion markers (from Fig. 3b) and using the changes in the surface chemical potential induced by hydrogen in the Kelvin probe method (from Fig. 3a) are in perfect agreement with each other.

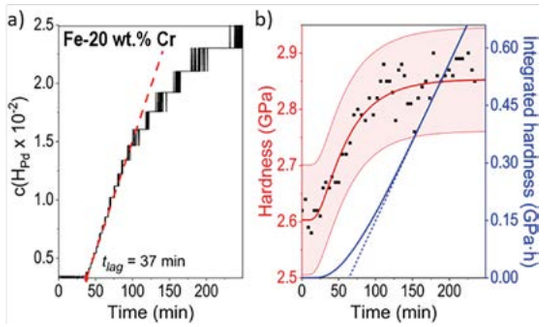

Fig. 3: *Comparison of the (a) permeation curves for the calculation of the diffusion coefficient based on the KP method; and (b) the calculation of the diffusion coefficient based on the hardness evolution during hydrogen loading. The light red region indicates the 95 % confidence band for the simulated hardness curve.*

In addition, charging the Fe-20 wt.% Cr alloy with hydrogen has a dual effect on its pop-in load under nanoindentation (Fig. 4a). Hydrogen reduces the pop-in load under a small indenter radius (Fig. 4b), e.g. *R*=170 nm, whereas it increases the pop-in load for larger indenter tips, e.g. *R*=4200 nm. The stress-dependent phase diagram of nanohydrides in this alloy reveals that for a small nanoindenter tip radius, the compressive stress under the indenter is high enough to induce the formation of nanohydrides (Fig. 4c). Their formation, associated with shear eigenstrain, facilitates the homogeneous nucleation of dislocations and leading to a decrease of the pop-in load. However, for larger indenters, the compressive stress induced is far too low to trigger the abovementioned mechanism. This means that the effect of hydrogen atoms will be limited to the formation of nano-hydrides close to pre-existing dislocations, pinning them and leading to an increase in the pop-in load. It is also shown by density-functional theory calculations that the reduction in the Cr content hinders the formation of nano-hydrides such that the hydrogen uptake and pinning effects are lowered.

References

1. Hachet, G.; Tehranchi, A.; Shi, H.; Prabhakar, M.; Wei, S.; Angenendt, K.; Zaefferer, S.; Gault, B.; Ponge, D.; Raabe, D.: arXiv.2407.03763 (2024).
2. Duarte, M.J.; Fang, X.; Rao, J.; Krieger, W.; Brinckmann, S.; Dehm, G.: J. Mater. Sci. 56 (2021) 873 2.
3. Rao, J.; Lee, S.; Dehm, G.: Duarte, M.J.: Mater. Design 232 (2023) 112143 .

Barrier coatings against hydrogen embrittlement

M.J. Duarte[1], A. Kanjilal[1], M. Palm[1], H. Gopalan[1], J. Rao[1], B. Gault[2], J. Zavašnik[3,4], G. Dehm[1], C. Scheu[5]

[1]SN, [2]MA, [3]Max Planck Partner Group, [4]Jozef Stefan Institute, Ljubljana SL, [5]NG

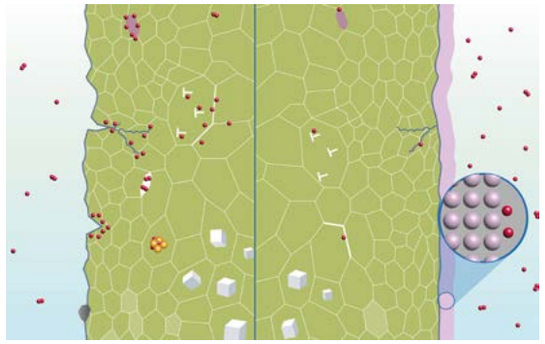

Fig. 1: *Schematic of hydrogen-metal interactions and the advantage of using hydrogen barriers.*

In the battle against hydrogen embrittlement, barrier coatings emerge as an important solution to limit hydrogen ingress into structural materials, such as those used for hydrogen transport and storage, thereby preventing failure. These coatings are primarily ceramics, such as oxides, nitrides, or carbides, with remarkably low hydrogen permeation [1] and technological maturity to be deposited or grown on various surfaces. Additionally, their cost is relatively low compared to other advanced materials. Our research on barrier coatings started in 2020, focusing on oxide films as barriers against hydrogen ingress into ferritic steels and iron alloys [2, 3]. Further studies extended to other ceramic coatings, such as nitrides, and to different steel and aluminum alloys as substrates.

Alumina, or aluminum oxide (Al_2O_3), is a prime candidate for hydrogen barrier coatings due to its low hydrogen permeability. Its performance is intrinsically linked to the coating microstructure, the presence of defects, and its thermal and mechanical stability. The permeation reduction factor (PRF) of alumina also varies depending on the coating thickness, deposition process, and operating conditions like temperature and pressure. Its PRF values range from tens to hundreds for thin films, and up to thousands for thicker or high-quality structured alumina coatings. Nevertheless, a significant engineering obstacle is the adhesion of alumina to metal substrates, especially those used in environments with varying temperatures, since differences in the thermal expansion coefficient can lead to spallation of the coating.

Our initial studies involved plasma ion-assisted deposition of amorphous Al_2O_3 films, < 2 µm thick, on a Fe-Cr alloy. This research was part of the project H2BS. The mechanical properties of the coating, the substrate, and their interface were tested by *in situ* nanoindentation and nanoscratching during hydrogen charging using a unique setup developed in-house (Fig. 2a) [3]. Kelvin probe tests revealed a low hydrogen diffusivity in the coating at room temperature, ~10^{-19} m^2s^{-1}. This is 9 orders of magnitude lower than in the substrate. The slow hydrogen diffusion in Al_2O_3 leads to the accumulation of hydrogen at the coating/substrate interface in backside charging conditions. This hydrogen enrichment drastically alters the scratch morphology of the coating and its adhesion to the substrate (Fig. 2b). Notably, the scratch-induced cracking behaviour recovered to its original state after hydrogen was released from the interface under ambient conditions. Nevertheless, hydrogen could still be detected in the coating by atom probe tomography several weeks later (Fig. 2c).

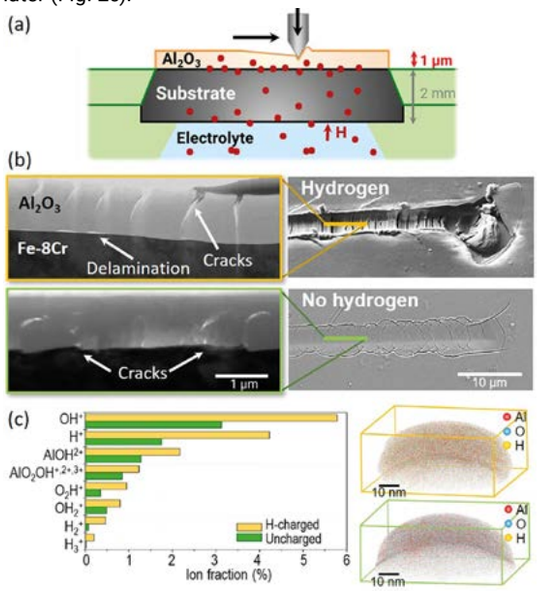

Fig. 2: *(a) Schematic of the nanoscratching process during in situ hydrogen charging. (b) Cross-section scanning transmission electron microscopy (STEM) images (left) showing different cracking behaviour of the Al_2O_3 coating after nanoscratching without and during hydrogen charging. The top view SEM images (right) reveal earlier cracking and delamination in the hydrogen charged case. (c) The higher content of hydrogen ion species, measured by atom probe tomography, confirms the presence of hydrogen in the coating near the interface with the substrate. The images are adapted from [3].*

In a second project, HEPCO (see p. 92), novel Al_2O_3 coatings are being developed through an innovative surface treatment technology based on electrochemical oxidation (ECO) of the underlying Al alloy substrate. The resulting microstructure of the coating constitutes crystalline nano-ceramic layers of Al_2O_3. The objective is to optimize the microstructure and thickness of the coating to achieve a PRF~1000 while ensuring high hardness and fracture toughness. Al_2O_3 coatings of different thicknesses were synthesized on a commercial aluminum alloy, susceptible to hydrogen embrittlement. By reducing the coating thickness, the microstructure changed from a mixture of α + η-Al_2O_3 phases in the thickest 30 µm coating to primarily η-Al_2O_3 phase for the 15 µm thick coating, confirmed by X-ray diffraction (XRD). Furthermore, the Al_2O_3 layer has a rather dense microstructure with uniform thickness and bonding at the coating-Al substrate interface and some degree of porosity and cracks (Fig. 3).

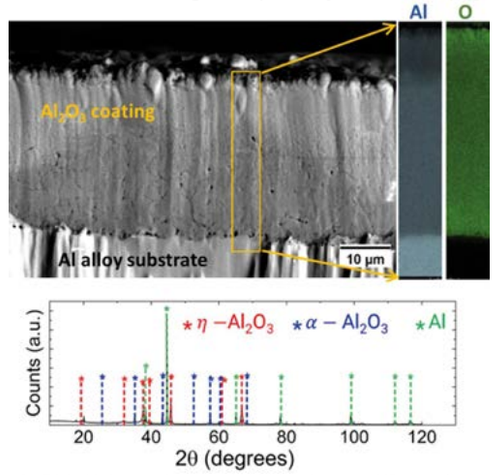

Fig. 3: *ECO-Al_2O_3 coatings on Al6082 substrate: XRD analysis of the 30 µm thick coating reveals two Al_2O_3 phases, while microstructural and SEM-EDS composition analyses of the coating cross-section show a dense microstructure and uniform distribution of Al and O.*

Self-forming superficial oxides are an affordable alternative to protect large-scale structural components, e.g. for hydrogen storage, manipulation, or transport. In collaboration with the partner group from Jožef Stefan Institute (Ljubljana, Slovenia), we investigate the hydrogen barrier properties of oxide thin films and their performance upon exposure to hydrogen, elevated temperatures, or a combination of both. Our main research method is the gas-permeation approach, a good proxy for bulk samples that considers the effect of grain size, grain boundaries, and overall microstructure contributions. This experimental system allows for *in situ* oxidation and heating of samples and is particularly useful for evaluating *in situ* formed oxide layers. Using this method, we assess bulk properties, phase transformations, and the oxide layer stability upon exposure to reducing or oxidizing atmospheres and/or up to 600 °C. The method is employed in joint collaborations to evaluate the barrier properties of various systems.

Using this route, we evaluated the self-forming alumina layers that form upon exposure to air on the surface of Fe-aluminides [4]. As a representative material of its class, we measured the hydrogen permeation rate for the B2-ordered Fe_3Al alloy, Fig. 4. The formation of a superficial alumina layer strongly depends on the phase composition of the alumina, with α-Al_2O_3 being the most effective hydrogen barrier. The phase transition of γ-Al_2O_3 to α-Al_2O_3 occurs between ~1000 - 1250 °C, a critical transformation for achieving the high-density and stable α-alumina phase. Through controlled oxidation of the Fe-Al samples, we obtained continuous and stable nm-thick alumina layers at temperatures < 500 °C. These layers exhibited permeation below the detection limit of our experimental setting, indicating an exceptional reduction in hydrogen ingress.

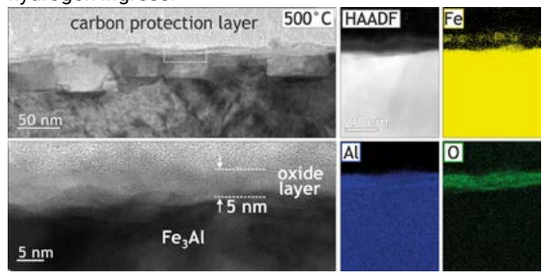

Fig. 4: *Polycrystalline α-Al_2O_3 layer developed on the surface of B2-ordered Fe_3Al upon exposure to air at T = 500 °C. EDS analysis shows Fe incorporation at the initial stages of oxidation.*

One more system under study is the engineering ceramic coating of titanium aluminum nitride (TiAlN), well-known for its excellent chemical stability, mechanical and thermal properties, and high hydrogen barrier efficiency. The hydrogen diffusion can be further reduced by controlled oxidation, which improves coating density and decreases permeability. TiAlN coatings are deposited by high-power impulse magnetron sputtering on Eurofer substrates. Our experiments involve multiple hydrogen permeation and oxidation cycles at room and elevated temperatures, evaluating the coatings' effectiveness in blocking hydrogen permeation. These cycling oxidation processes have been used to enhance barrier properties, achieving high PRF of up to 6000. However, severe degradation over repeated cycles, such as chemical and microstructural changes in the coating, has highlighted the critical need to stabilize the TiAlN coating to be usable as a hydrogen barrier. This stabilization is essential to maintain its effectiveness and ensure long-term durability under cyclic conditions.

References

1. Wetegrove, M.; Duarte, M.J.; Taube, K.; Rohlof, M.; Gopalan, H.; Scheu, C.; Dehm, G.; Kruth, A.: Hydrogen 4 (2023) 307.
2. Hieke, S.W.; Frank, A.; Duarte, M.J.; Gopalan, H.; Patil, P.; Wetegrove, M.; Rohloff, M.; Kruth, A.; Pistida, C.; Dornheim, M; Taube, K.; Dehm, G.; Scheu, C.: Adv. Eng. Mater. 26 (2024) 2300619.
3. Gopalan, H .; Rao, J.; Patil, P.; Jung, C.; Kim, S.-H.; Goodrich, S.; Wetegrove, M.; Kruth, A.; Scheu, C.; Dehm, G.; Duarte, M.J.: J. Mater. Res. 39 (2024) 1812.
4. Zavašnik, J. ; Peng, J.; Palm, M.: Corros. Sci. 179 (2021) 109170.

Atomistic mechanisms underlying hydrogen-based reduction of iron oxides

X. Zhou[1], B. Bienvenu[2], B. Gault[1], A. Abdelkawy[2], H. Chen[2], M. Todorova[2], C. Freysoldt[2], J. Neugebauer[2], D. Raabe[1]

[1]MA, [2]CM

As demand for iron and steel continues to grow towards annually 1.9 billion tons, the steel industry needs to move to less CO_2-intensive processes, which currently account for 8 % of global emissions. As an alternative to traditional carbon-based blast furnaces, the hydrogen-based direct reduction (HyDR) process is being investigated at MPI-SusMat. This highlight focuses on iron oxides, which represent the majority of ores from which iron is extracted. In traditional blast furnaces, CO acts as the reducing agent in an exothermic solid-to-melt reaction. Switching to H_2 in direct reduction reactors as reducing agent, there is no excess heat, and one operates below the melting temperature of iron. With a change to a solid-to-solid reaction, the role of the microstructure and its dynamic evolution during the reduction is of paramount importance in understanding the HyDR process of iron oxides. In order to bring the process up to the industrial scale, the fundamental mechanisms underlying the HyDR process need to be studied at different scales, from the atomic and electronic structure scale to the reactor scale, using both experimental and theoretical tools. Hereby, we pursue a number of avenues, refining and developing the methods we use as necessary.

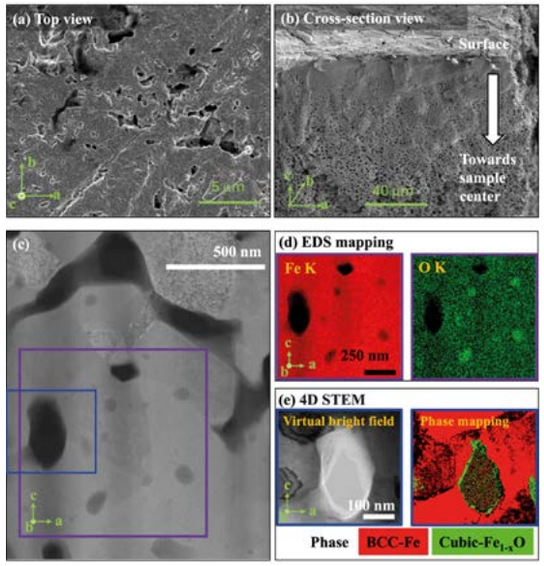

Fig. 1: *Microstructure of $Fe_{1-x}O$ sample after partial hydrogen-reduction at 700°C [1]. Scanning electron microscopy (SEM) images of the (a) top and (b) cross-section views. (c) High-angle annular dark-field (HAADF) image of a region of the sample close to pores. (d) EDS mapping of the purple region in (c) for the Fe K and O K edges. (f) 4D STEM reconstruction of the blue region in (c) showing the virtual bright field image and phase mapping.*

Based e.g. on the knowledge gained at MPI-SusMat in recent years, we have been able to identify key scientific questions that will ultimately contribute to the understanding of the HyDR process. The effect of the microstructure on the elementary redox processes, the interplay between the two and the mass transport of iron and oxygen mediating the phase transformations occurring during reduction have been identified as bottlenecks of the reaction kinetics. In order to study these phenomena and to understand the basic mechanisms related to the above key questions, we combine experimental work carried out in the MA and GO departments with theory and simulation work in the CM department.

In order of decreasing oxygen content, iron oxides occur mainly as three minerals: hematite (Fe_2O_3, 60 at. % of oxygen), magnetite (Fe_3O_4, 57 % of oxygen) and wüstite ($Fe_{1-x}O$, where x (≈5 %) quantifies the depletion of the Fe sublattice). The successive reduction of these oxides to pure Fe is accompanied by a drastic loss in volume, which drives the formation of structural defects such as dislocations, cracks and pores. As an example, Fig. 1 a-c shows the microstructure of a wüstite ($Fe_{1-x}O$) sample partially reduced with hydrogen [1]. After reduction, the sample exhibits a wide range of structural defects such as interfaces between different phases and pores. The latter arise from the volume loss that the sample must undergo from the oxides to metallic iron (approximately 40 % from $Fe_{1-x}O$ to Fe).

The energy dispersive X-ray spectroscopy (EDS) analysis shown in Fig. 1 d reveals that some regions near the closed pores show a higher intensity in the O K map, accompanied by darker contrast in the Fe K intensity map, indicating that reoxidation has occurred close to the pore. This has been further validated by the phase mapping from the four-dimensional scanning transmission electron microscopy (4D STEM) reconstruction (see Fig. 1.e), in which the $Fe_{1-x}O$ phase appears on the surface of closed pores. This immediately highlights the importance of the interplay between elemental redox processes and microstructural changes in comprehending the kinetics of the hydrogen reduction process.

As the oxides are gradually reduced to pure iron, interfaces form between different phases. The interfaces act as barriers to the transport of iron, oxygen, and hydrogen, limiting the efficiency of the process. In a recent joint experimental-theoretical study, we investigated the atomic structure of the interface between iron and magnetite [2]. Using differential phase contrast imaging in a STEM, we were able to identify a peculiar well-ordered reconstruction of the interface (referred to defect phase or complexion) with a FeO-like structure. Fig. 2 shows both the experimental images and the density functional theory (DFT) structure of the Fe/Fe_3O_4 interface, highlighting the excellent agreement found between the two methods when a two-layer thick FeO slab is inserted between the Fe and Fe_3O_4 slabs (see the structure on the right between the experimental and DFT-computed charge densities, denoted by (v)).

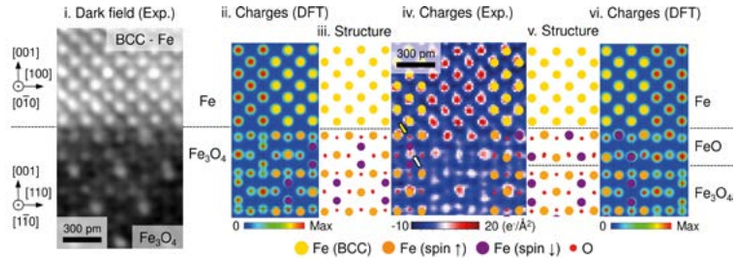

Fig. 2: *The Fe(001)/Fe_3O_4(001) interface [2]: (i) virtual dark-field image and (iv) charge-density map, along with two sets of DFT calculations comprising charge-density maps (ii & vi) and relaxed structures (iii & v). The hypothetical pristine interface (ii & iii) deviates from experiment (see arrows). The interface with a reconstructed two-layer FeO slab (v & vi) agrees well.*

Using DFT-based thermodynamics, we constructed the phase diagram of the iron/magnetite interface and showed that FeO-like defect phases are more stable than the clean Fe/Fe_3O_4 interface over a wide range of chemical potentials. These defect phases will play an important role in the transport properties of iron and oxygen across these interfaces, thus strongly influencing the redox kinetics in presence of these defects.

However, the atomistic modelling of iron oxides poses major challenges to DFT calculations, due to their combined structural and electronic complexities. These became apparent when we began to map out the potential energy surface (PES) for H diffusion in the bulk of hematite. The strong correlations within the magnetic structure of the iron oxides presented an obstacle to obtaining a smooth PES. Small changes in the H position could trigger a transition between metastable electronic states, and revealed our inability to achieve a controlled description of the electronic and magnetic configurations, resulting in discontinuities in the energy landscape. To address this issue, we are currently developing an improved Hubbard U correction to enable a targeted and controlled description of correlative effects in the electronic structure.

However, even when this goal is achieved, DFT calculations cannot address long length and time scales. Some of the features observed experimentally, such as the formation of pores at the metal-oxide interface, are too large to reasonably fit within the confines of a supercell accessible to electronic structure calculations. To overcome such scale limitations of DFT, we have recently developed a machine-learned interatomic potential based on the Atomic Cluster Expansion (ACE) for the binary Fe-O system [3]. The ACE model has been fitted to an extensive database of DFT calculations (for now, at the level of the Perdew-Becke-Ernzerhof exchange-correlation functional) including pure iron and a wide range of possible oxygen-containing structures, also including magnetic degrees of freedom. By allowing for three different magnetic states of iron within the model – one neutral Fe species and two Fe species with opposite spins – the obtained ACE potential correctly describes the magnetic structure within the three major iron oxides – hematite, magnetite and wüstite. It also reproduces surface structures, and follows the evolution of iron oxide nanoparticles as a function of increasing oxygen chemical potential, by means of their respective Wulff shapes. Through extensive validation, we demonstrated the accuracy and transferability of the ACE potential for a wide range of properties of iron and its oxides, showing very good agreement with DFT and experimental references. The potential now enables us to study directly at the atomic scale some of the fundamental mechanisms involved in the HyDR process, such as the formation of pores or the behaviour of structural defects, by performing dynamic simulations where both atomic positions and magnetic degrees of freedom can evolve simultaneously.

To better understand the transformation processes during reduction, it is also crucial to combine insights into the crystallographic structure with the composition of the different phases and their interfaces at the near-atomic scale. Experimentally, this can be achieved by combining transmission electron microscopy (TEM) and atom probe tomography (APT), as demonstrated in a recent pioneering work at MPI-SusMat [1]. This study involved *near-in-situ* reduction of oxides using the laser-enabled ReactHub Module [4]. The accuracy of APT analyses of oxides is hampered by a dependence on the electric field, which can activate the dissociation of the emitted metastable molecular ions into neutral O_2 molecules, which may go undetected. A systematic study was performed jointly by the MA and CM departments to evaluate the performance of APT for the analysis of FeO, Fe_2O_3 and Fe_3O_4 [5], which showed that it is in principle possible to distinguish the different oxides by using the ratio of charge states as an additional descriptor.

References

1. Zhou, X.; Bai, Y.; El-Zoka, A.A.; Kim, S.H.; Ma, Y.; Liebscher, C.H.; Gault, B.; Mianroodi, J.R.; Dehm, G.; Raabe, D.: Phys. Rev. Lett. 130 (2023) 168001.
2. Zhou, X.; Bienvenu, B.; Wu, Y.; Kwiatkowski da Silva, A.; Ophus, C.; Raabe, D.: arXiv:2408.09213.
3. Bienvenu, B.; Todorova, M.; Neugebauer, J.; Raabe, D.; Mrovec, M.; Lysogorskiy, Y.; Drautz, R.: arXiv:2407.13903.
4. El-Zoka, A.A.; Stephenson, L.T.; Kim, S.H.; Gault, B.; Raabe, D.: Adv. Sci. 10 (2023) 2300626.
5. Kim, S.H.; Bhatt, S.; Schreiber, D.K.; Neugebauer, J.; Freysoldt, C.; Gault, B.; Katnagallu, S: New J. Phys. 26 (2024) 033021.

Basic mechanisms behind sustainable metallurgical reduction processes

M. Jovičević-Klug[1], Ö. Özgün[1], S. Sahu[2], B. Bienvenu[3], I. Souza[1], J.P. Best[2], D. Raabe[1]

[1]MA, [2]SN, [3]CM

Sustainable metallurgical reduction of oxides is one of the building blocks for mitigating CO_2 impact of the industrial sector. In particular, the primary reduction of iron oxides to iron is one of the main contributors, accounting of about 70 % of the total CO_2 emissions from the steel industry sector. Inevitably, transition towards sustainable carbon-free reducing media, such as hydrogen, is a necessity to achieve the set goals of the Paris agreement. Consequentially, a deep understanding of the rudimentary mechanisms during iron oxide reduction is crucial for proper transition and upscaling of novel reduction processes on a global scale.

Pressure influence and hydrogen trapping in HyDR

Hydrogen-based direct reduction (HyDR) is the most compelling strategy to produce green steel. HyDR is a multistep solid-state reduction scheme (Fig. 1a), where iron ores, usually hematite or magnetite, are reduced to iron at high temperatures of 500-1100 °C. H_2 reacts with the chemically bound oxygen, reducing the iron's oxidation state, i.e., from hematite (Fe_2O_3) to magnetite (Fe_3O_4), wüstite (FeO) and metallic iron (Fe). During HyDR, pores evolve due to the removal of oxygen and crack formation that profoundly influence the reduction kinetics. The H_2 partial pressure also significantly affects reduction kinetics and thus the microstructure evolution of reduced pellets [1-3]. In our study, we investigated the effect of the overall H_2 gas pressure on the reduction kinetics of Fe_2O_3 pellets. Our results showed an increase of the overall reduction kinetics with hydrogen gas pressure, Fig. 1a. Resultingly, the pore structure in the reduced pellet transformed, from elongated (i.e., at 1 bar), Fig. 1b, to the random-shape pore structure (i.e., at 50 bar), Fig. 1c.

Another perspective in the hydrogen-based reduction schemes, both HyDR and liquid-state based hydrogen plasma smelting reduction (HPSR), is the amount of trapped hydrogen in the final product. Particularly, this has raised concerns as already a few ppm of hydrogen in steels can lead to mechanical instability originating from hydrogen embrittlement [4]. We explore this, by applying thermal desorption spectroscopy to evaluate the hydrogen content in iron produced via HyDR and HPSR [5]. Fig.1d presents that direct reduced iron traps ~40 wppm of hydrogen that with subsequent melting in the arc furnace is drastically reduced to 1-2 wppm, following similar values of the HPSR reduced material (~1 wppm). The results clearly indicate that green steel produced using hydrogen-based ironmaking achieves similar hydrogen levels (1-2 wppm) as steel made through conventional processes (5-10 wppm), proving that sustainable hydrogen-based reduction schemes do not impose risks for hydrogen embrittlement.

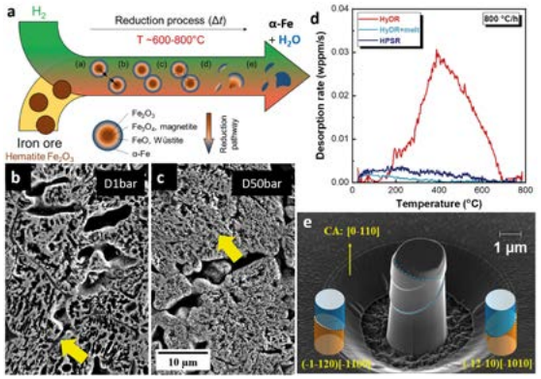

Fig. 1: *a) Schematic presentation of the stepwise iron oxide reduction to iron via HyDR. Microstructure of Fe_2O_3 pellets reduced at 700 °C at b) 1 bar and c) 50 bar. d) TDS spectra of the desorption rate of hydrogen from HyDR, HyDR+melt, and HPSR samples. e) Micropillar compression of Fe_2O_3 phase, with SEM micrograph shows the active deformation systems at RT.*

Phase transformation derived stress mechanics in HyDR

Contemporary solid-state reactors encounter significant challenges, including formation of a reaction layer on the outer surface, inhomogeneous transformations and reaction progression. This often results in an unreacted Fe_2O_3 core, undermining process efficiency. Additionally, the phase transformations governed volume and stress changes complicate the local mechanical response of the iron oxide phases. Future reactors must encompass controlled fracture and delamination at the metal/oxide interface to control the reaction rates and promote complete conversion to metallic iron. Howbeit, a considerable knowledge gap remains on the micromechanical properties of iron oxide phases at elevated temperatures (600-800 °C). The FeOx-HOTMECH project, funded by the KSB Foundation since 2022, aims to elucidate aforementioned topic using nanoindentation and micropillar compression techniques. Furthermore, the brittle-to-ductile transition through microcantilever fracture analysis is also investigated and linked to plasticity mechanisms.

Significant insights have been gained into the microscale plastic deformation of single crystals through electron backscattered diffraction and transmission electron microscopy (see Fig. 1e). Hematite's trigonal symmetry manifests in various modes of deformation, including basal, prismatic, pyramidal slip, as well as rhombohedral and basal twinning. In contrast, cubic FeO deforms solely through {111} <1-10> slip at room temperature, determined using micropillar compression. The critical resolved shear stress (CRSS) of the most readily deformable mode in Fe_2O_3 was quantified at 1.6 GPa, more than double the CRSS of FeO. The experiments at room temperature effectively illustrate the influence of crystal symmetry on plasticity, with Fe_2O_3 requiring the activation of multiple deformation modes for general homogeneous deformation, whereas FeO can accommodate this solely through the activation of one slip system family. This heightened plasticity significantly complicates fracture behaviour along interfaces of higher-order reduced phases, such as Fe_3O_4-FeO, which strongly affects the reduction efficacy [3]. Such analyses are critical for understanding microscale contact mechanics during the solid-state reduction of iron ores.

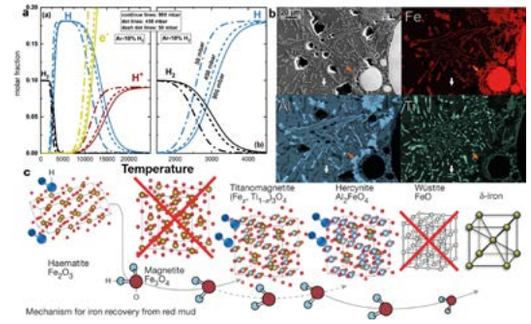

Fig. 2: *a) Equilibrium calculations for Ar-10 % H_2 gas mixture at 50 mbar, 450 mbar and 900 mbar displaying the hydrogen-related plasma species. b) Micrograph of reduced red mud material and accompanying chemical maps of Fe, Al and Ti. c) Chemical mechanism for iron recovery from red mud with hydrogen plasma reduction.*

Processing gas parameters influence on HPSR

For many complex oxides, extending beyond single phase iron oxides, their chemical construct can modify and significantly hinder the full or partial reduction to extract precious metals [2]. To overcome the diffusion-related thermodynamic limitations, HPSR utilizes the simultaneous melting of the oxide and reduction with excited hydrogen species (i.e. plasma). Such specific combination enables access to fast kinetics and chemical partitioning that is otherwise unobtainable through solid-state reduction processes, such as HyDR [6]. However, the efficiency in metal extraction through HPSR is significantly dependent on the processing conditions. The utilization of lower pressures strongly enhances the dissociation potentials of the molecular hydrogen molecules into atoms and ions due to the reduced gas density (Fig. 2a). Consequentially, this delivers higher reduction potentials and rates that result in more efficient hydrogen utilization. On the other hand, with higher concentration of hydrogen in the argon-based gas mixture, i.e. increasing from 10 % to 20 %, further improves the reduction kinetics. However, consequently the plasma temperature significantly increases that induces higher evaporation of the newly formed metal. In the case of Fe_2O_3 reduction with 20 % H_2, the metal loss through evaporation is increased 3.5-fold against the 10 % H_2 case, resulting in evaporation of nearly 70 % of the initial iron contained in hematite [7]. This example indicates the profound necessity to understand the influence of HPSR processing parameters for optimal oxide reduction and metal extraction.

Reduction of mixed oxides

In addition to the improved kinetics, HPSR provides the opportunity to open reduction pathways of oxides beyond single metal oxides such as high-grade Fe_2O_3 and Fe_3O_4 ores. This allows extending reduction to unconventional feedstocks and sources for obtaining pure metals from otherwise unusable mixed oxides and compounds. The recent research on extracting iron from red mud using HPRS [8], highlights the versatility and efficiency of the process. The red mud is melted and with reduction partitions into iron rich melt and a residual oxide melt. The latter during solidification chemically partitions into an intricate ensemble of chemically well-defined oxide crystalline phases that are rich in Fe, Al, Ti that reside in the amorphous Si, Ca and Na rich amorphous matrix (Fig. 2b). This is enabled by the strongly altered chemical pathway (Fig. 2c) to metallic iron through reduction that allows the substitutional elements, i.e. Al and Ti, from the complex oxides to separate into their individual phases that over time coalesce and grow. As a consequence, HPSR enables macroscopic partitioning of individual valuable oxide species, i.e. Ti oxides, that can be potentially utilized as feedstocks in subsequent processes.

In order to understand the hydrometallurgical or electrochemical potential of using the final Ti-rich oxides, density functional theory calculations were performed. Along the hydrogen reduction process, different Ti-rich compounds appear in the microstructure (Ti_xO_y, and in particular TiO_2, Ti_2O_3 and Ti_3O_5) and mixed oxides containing Ti (e.g. Fe_5TiO_8, $FeTiO_3$, $CaTiO_3$ or $FeMgTi_4O_{10}$) [8]. For each compound, the equilibrium structure and magnetic order was determined, from which the heat of reaction for the extraction of pure Ti was performed from their hydrogen reduction through multiple reaction paths, also considering different well-established processes (such as the Kroll and Hunter processes). Focusing at first only on the stable pure Ti oxides, we find that their hydrogen reduction is easily achievable, with a successive decrease in the oxygen content from TiO_2 to Ti_2O_3 to Ti_3O_5. Further work to scan through all possible chemical reactions, also including mixed Ti oxides, will allow to determine possible routes for extracting Ti from the various compounds found during the reduction of red mud samples, and asses their relative ease.

References

1. Özgün, Ö.; Dirba, I.; Gutfleisch, O.; Ma Y.; Raabe, D.: J. Sustain. Met. (2024). doi.org/10.1007/s40831-024-00877-4
2. Spreitzer, D.; Schenk, J.: Steel Res. Int.90 (2019) 1900108.
3. Ma, Y.; Souza Filho, I. R.; Bai, Y.; Schenk, J.; Patisson, F.; Beck, A.; van Bokhoven, J. A.; Willinger, M. G.; Li, K.; Xie, D.; Ponge, D.; Zaefferer, S.; Gault, B.; Mianroodi, J. R.; Raabe, D.: Scr. Mater. 213 (2022) 114571.
4. Johnson, W. H.: Nature 11 (1875) 393.
5. Özgün, Ö.; Lu, X.; Ma, Y.; Raabe, D.: npj Mater. Degrad. 7 (2023) 7
6. Souza Filho, I. R.; Ma, Y.; Kulse, M.; Ponge, D.; Gault, B.; Springer, H.; Raabe, D.: Acta Mater. 213 (2021) 11697
7. Souza Filho, I.R.; Ma, Y.; Raabe, D.; Springer, H.: JOM 75 (2023) 2274.
8. Jovičević-Klug, M.; Souza Filho, I.R.; Springer, H.; Adam, C.; Raabe, D.: Nature 625 (2024) 703.

Deciphering reactions at electrochemical solid/liquid interfaces: Mg dissolution under anodic conditions

M.Todorova[1], Z. Wang[1], F. Deißenbeck[2], S. Wippermann[2], C. Freysoldt[1], J. Neugebauer[1]

[1]CM, [2]GO

Reactions that occur at the interface between a solid and a liquid are at the heart of many applications that are central to achieving a sustainable future. The significant impact of such reactions is typically observed on a macroscopic scale, but they are initiated at the level of atoms and molecules, where they are strongly influenced by the local environment in which they occur. A prime example of such a reaction, which has puzzled corrosion scientists to this day, is the corrosion of Mg under anodic conditions. Ever since the first observation of the enhanced Mg dissolution occurring at anodic conditions and the unexpected violent evolution of H_2 which goes hand in hand with it, there have been various attempts to rationalise these observations. Probably one of the most controversially discussed theories in this context is the suggestion for the existence of a unipositive Mg ion [1], i.e. Mg^+. Although such a species contradicts common chemical understanding, it would be capable of explaining the experimentally measured amount of dissolved Mg, which is greater than coulometrically expected by invoking the conventional dipositive Mg^{2+} ion. Furthermore, it has been shown that these elusive unipositive species have a lifetime of several minutes in aqueous solution and reduce other species at macroscopic distances away from the Mg anode. However, all this evidence is indirect and experiments that clearly distinguish different oxidation states, such as atomic emission spectroelectrochemical experiments, only find evidence for Mg ions in the expected charge state, i.e. Mg^{2+}. Clearly, such a situation can only be resolved by microscopic observations of the reactions and processes taking place at the Mg/H_2O interface under anodic conditions. Performing *ab initio* molecular dynamics (AIMD) calculations using our well-proven electrochemical cell setup [2] and recent thermopotentiostat approach [3] seemed to be a natural choice to explore possible reactions.

AIMD calculations we had previously performed on the basal Mg (0001) surface allowed us to identify the mechanism by which hydrogen evolves from the surface under anodic conditions, but as expected no dissolution events occurred. Bearing in mind that dissolution is generally understood to proceed via kink atoms, as the one most loosely bound to a surface, we set up the supercell using a 6-layer Mg slab with a (1 2 -3 15) vicinal surface (with 2 kink sites) exposed to explicit water.

We first ran the AIMD calculations without potential control (open circuit conditions). We observed, similarly to the flat Mg(0001) surface, water dissociation events leading to the formation of OH groups adsorbed on the surface. Not unexpectedly, such dissociation events occur at and in the vicinity of the kink site and we consistently find an OH group adsorbing at the hollow site adjacent to the kink. Although this makes the kink atom even more positive we do not observe Mg dissolution under open circuit conditions. Dissolution only occurs after we turn on the potential control and anodically polarise the surface, i.e. make it electron deficient. The Mg kink atom makes several attempts to detach from the surface, but only succeeds after a water molecule creeps into the space between the detaching Mg kink atom and the Mg surface, thereby hindering it to re-attach. This results in the Mg kink atom being surrounded by 5 water molecules, forming an almost complete solvation shell (consisting of 6 water molecules). Charge analysis furthermore reveals that the kink atom has also transferred two of its electrons to the surface, thereby becoming a Mg^{2+} ion. However, this Mg^{2+} ion remains bound to the surface being anchored to it by the OH group. The binding energy of this $[Mg^{2+}\ OH^-]^+$ complex is of the order of 2 eV, making it particularly stable. It can therefore be concluded that it is not the formation of the Mg ion, i.e. the transfer of the two Mg electrons to the surface, but rather the breaking of the hydroxyl bridge bond to the Mg surface that is the rate-limiting step in the dissolution reaction.

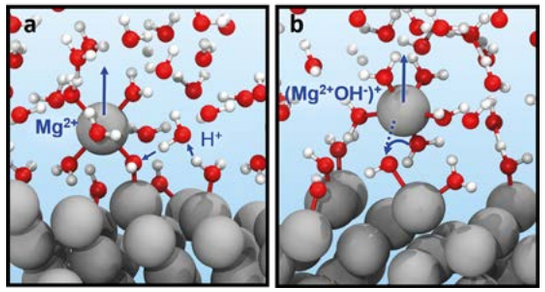

Fig. 1: *A Mg ion dissolving from a Mg (1 2 -3 15) surface in contact with water. The dissolution may proceed via (a) a double proton transfer, which leads to the dissolution of a Mg^{2+} ion and leaves a OH group at the surface and (b) via a intra-solvation-shell proton transfer, which leads to the dissolution of a $[Mg^{2+}OH^-]^+$ complex and leaves a pristine kink site behind.*

Our calculations revealed two possible reaction pathways by which this could happen [4]. The first one involves a double proton transfer (Fig. 1a) from a water molecule adsorbed on the surface via a solvated water molecule in its vicinity, which is also bonded to the OH-group anchoring the Mg^{2+} ion by a H-bridge. This process adds a proton to the OH group, forming a water molecule and completing the solvation shell of the Mg^{2+} ion, which now contains the required 6 water molecules.

This mechanism allows the Mg^{2+} ion to dissolve and move rapidly away from the surface into liquid water, but an OH group remains on the Mg surface, albeit moved laterally to an adjacent position. This mechanism will therefore quickly passivate the Mg surface, by hydroxylation. It is therefore not suitable for sustaining enhanced dissolution and hydrogen evolution.

However, we also found a second mechanism by which the bond between the OH group and the Mg surface can be broken. This involves a proton transfer within the solvation shell of the Mg^{2+} ion (Fig. 1b), resulting in the dissolution of the entire $[Mg^{2+}OH^-]^+$ complex. This mechanism removes the OH group from the surface, exposing a pristine new kink site at which a water molecule can dissociate and trigger the described reaction cycle again. This reaction can be written as

$$Mg + H_2O \rightarrow [Mg^{2+}OH^-]^+_{aq} + (H^+ + e^-) \rightarrow [Mg^{2+}OH^-]^+_{aq} + \tfrac{1}{2} H_2.$$

The ratio of dissolved Mg to H is 1:1, explaining the coulometric measurement.

A particular challenge in observing the described reactions was to achieve a sufficiently high electric field at the Mg/water interface to trigger them. This was due to (i) the high screening capabilities of water, which reduces the strength of the field reaching the interface when the computational counter electrode (CCE) is further away from the working electrode, and (ii) the small vacuum region ensuing between the computational Ne electrode and the water. This is a consequence of the hydrophobic gap that forms between the two and has the effect of causing a significant fraction of the applied potential to drop within this region. To avoid this unwanted potential drop, we have started to develop a fully solvated electrode (FSE). It is, in complete analogy to the computational Ne electrode, an efficient and powerful surrogate model for the double layer on the side of the electrode facing away from the interface, but allows us to move the CCE closer to the interface, avoiding the hydrophobic gap and the unwanted potential drop within. So far, the FSE has been thoroughly tested with atomistic calculations using LAMMPS. Tests for its use with *ab initio* codes are currently underway.

We also aim to obtain the barriers for electron transfer reactions at electrochemical solid/liquid interfaces. The theory of charge-transfer reactions in a thermal bath was developed by Marcus already in the 1960s, but it employed empirical parameters that cannot be obtained from simulations easily: The challenge is to efficiently sample the high dimensional phase space of relevant degrees of freedom, notably the reorganization of the solvation shell, and project it to a suitable reaction coordinate. As a first step in this direction, we focused on two different states of an ion in bulk water. Consider, for instance, the transition between a neutral Na atom solvated in water and its ionic state Na^{1+}. By assigning an artificial fractional charge to the ion, we can systematically explore the phase space that links the two physical charge states. The artificial charge of the ion thus serves as the most suitable reaction coordinate for atomistic calculations, as it naturally activates the degrees of freedom responsible for adapting the screening upon charge transfer. In practice, we first create a number of pseudo-Na ions with charge states between 0 and 1, e.g. Na^0, $Na^{0.3+}$, $Na^{0.7+}$, Na^{1+}. For each of these ions we run molecular dynamic simulations. Using uncorrelated snapshots from a MD calculation associated with a particular charge state, we perform static calculations for the neutral Na atom and the Na^{1+} ion (Fig. 2). As a Na^0 (Na^{1+}) will be over-screened (under-screened) when embedded in the solvation shell corresponding to, for example, a $Na^{0.3+}$ ion, we ensure that an appropriate charge correction is applied to obtain the correct energy that a Na^0(Na^{1+}) will have when embedded in the $Na^{0.3+}$ solvation shell.

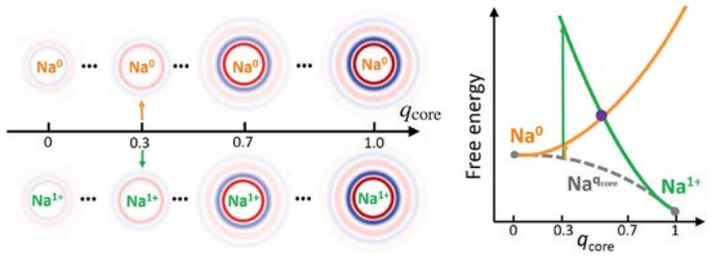

Fig. 2: *(left) Solvation shells obtained from molecular dynamics calculations for Na in charge states corresponding to q_{core}. These solvation shells are then used to calculate the energy for a neutral Na (Na^0) and a Na ion (Na^{1+}). (right) The obtained free energies corresponding to the respective q_{core} are used to construct "Marcus parabolas.*

Having thus obtained the energy that a Na will have as its solvation shell evolves from the neutral to the fully ionic charge state, we can construct the "Marcus parabola" associated with each of these states, i.e. Na^0 and Na^{1+}, by performing thermodynamic integration to align the energies . This gives us direct access to the barrier associated with the transition, both in terms of energy and geometry, and provides invaluable insights into the driving force for the charge transition. For the case considered here, we find that the transition occurs when the first solvation shell of the Na^{1+} ion is formed, while the minimum is reached when the second solvation shell is reached. Obviously, this barrier can be manipulated by applying a potential. Furthermore, having identified an appropriate reaction coordinate, we can now extend this work to include the solid/liquid interface. This is a crucial step towards developing an intuitive and efficient methodology to study reaction barriers at electrified electrochemical solid/liquid interfaces. Both of these directions are presently pursued.

References

1. Perry, R.L.; Davidson, A.W.; Kleinberg, J.: J. Am. Chem. Soc. 76 (1954) 363.
2. Surendralal, S.; Todorova, M.; Finnis, M.; Neugebauer, J.: Phys. Rev. Lett. 120 (2018) 246801.
3. Deissenbeck, F.; Freysoldt, C.; Todorova, M.; Neugebauer. J.; Wippermann, S.: Phys. Rev. Lett. 126 (2021) 136803.
4. Deißenbeck, F.; Surendralal, S.; Todorova, M.; Wippermann, S.; Neugebauer, J.: JACS 146 (2024) 30314–30319.

Grain boundary structure, decoration, and chemical composition

T. Brink,[1] X. Zhou,[2] S. Zhang,[3] C. Liebscher,[1] T. Hickel[4]

[1]SN, [2]MA, [3]NG, [4]CM

Grain boundaries (GBs) are interfaces between regions with different crystallographic orientations and are therefore ubiquitous defects in materials. They strongly affect macroscopic properties, including mechanical strength, embrittlement, diffusivity, and electrical/thermal conductivity. The idea of GB phases (or more generally, defect phases) is that the atomic structure of defects determines how they influence the macroscopic properties, enabling defect engineering. This is a research topic across our institute (see also p. 216,222,230). Here, we report on the atomic structure and chemical composition of GBs with atomic-resolution experiments and simulations.

We found that even simple [111] tilt GBs in pure fcc metals exhibit remarkable structural variety. In Cu [1] and Al [2] thin films, we found several GB phases and their defects by atomic-resolution scanning transmission electron microscopy (STEM) (Fig. 1). These can depend on the macroscopic GB parameters, i.e., the geometry of the GB, but even with the same geometry, different structures can occur (Fig. 1(a)). By performing atomistic computer simulations, we could elucidate both the 3D structure and the thermodynamics of the GB phases (Fig. 1(c)). Indeed, we show that the observed pearl and domino structures are universal across misorientations and different fcc metals and that GB phase transitions between them should be common [3].

The most pronounced effect on material properties is however expected due to segregation of additional elements to the GB. For segregation, often averaged thermodynamic models are proposed. In our work, we also consider the atomistic details of the segregation sites, which strongly affect the segregation itself. In a first work, we correlated STEM, energy dispersive x-ray spectroscopy (EDS), and atomistic simulations of Ag segregation to a Cu GB [4]. Clear segregation patterns were found with all methods and assigned to specific atomic structures (Fig. 2(a)). We reproduced this pattern with hybrid molecular dynamics (MD)/Monte Carlo (MC) simulations, which furthermore revealed a weak correlation between local free volume and preferred Ag segregation sites [4].

In Mg, a structural transition can be triggered by Ga segregation [5,6]. The structure of [0001] tilt GBs in this hcp material has been thoroughly characterized by STEM (e.g. Fig. 2(b)). Our MD and density functional theory (DFT) calculations provide a description of the thermodynamics of this transition, which is an example of a segregation-induced GB phase transition. As shown by our studies on segregation in Cu, the atomic structure of segregation sites clearly matters, so a co-evolution of structure and segregation leads to complex material behaviour, but also potentially enables defect engineering. Such systematic studies can be used to construct defect phase diagrams (see p. 222).

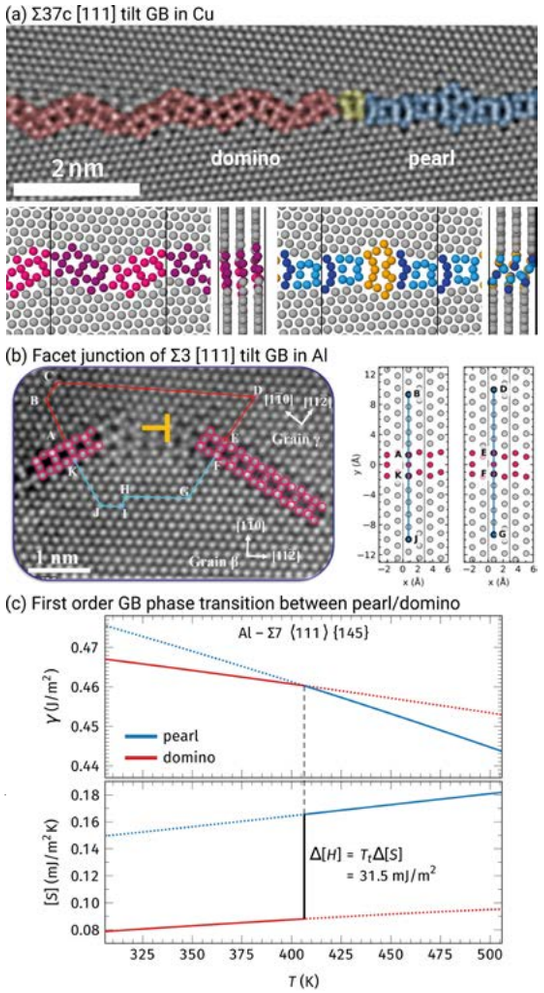

Fig. 1: *GB phases in fcc metals. (a) Two GB phases on the same GB in Cu. From [1]. (b) Analysis of a facet junction line defect on an Al GB. From [2]. (c) The transition between the domino and pearl structures is a first order transition with excess latent heat Δ[H], visible when plotting the GB excess entropy [S]. From [3]. All images used under CC BY 4.0 International.*

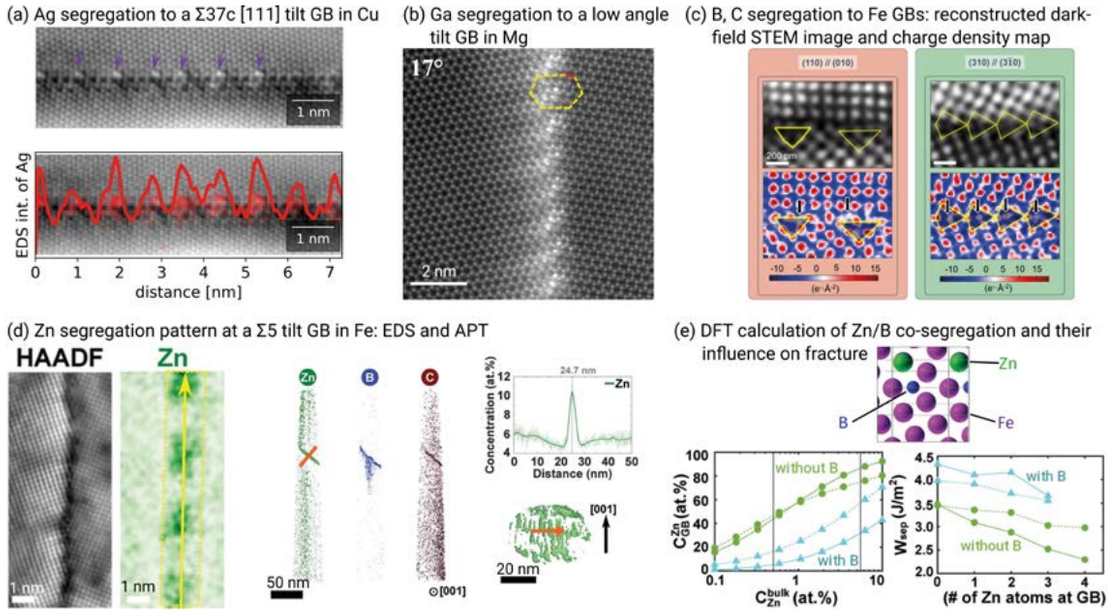

Fig. 2: *Segregation to GBs detected using experimental methods (a–c). From [4], [5], and [7]. (d–e) Investigation of the embrittler Zn in Fe GBs, and how this can be mitigated by B and C segregation. From [8]. Images used under CC BY 4.0 International, except (b) under CC BY 3.0 Unported.*

For Fe alloys, B and C are important impurities, but these light elements are difficult to measure. By utilizing advanced imaging techniques such as charge-density mapping and atom probe tomography (APT), we achieved direct visualization and quantification of these interstitial solutes at the GBs [7]. Our findings reveal that variations in the inclination of grain boundary planes, despite identical misorientation, significantly affect both the composition and the atomic arrangements at these GBs (Fig. 2(c)). This highlights once again the pivotal role of atomic motifs in controlling the chemical properties of GBs, thereby bridging a critical gap between the structure and chemical composition of these defects. To address the complexities inherent in the five degrees of freedom of GBs, we developed a workflow involving the growth of bicrystals with consistent crystal orientations but varying GB planes and a specialized code that enabled the observation of light elements within the GBs [7].

These results become relevant for liquid metal embrittlement, where GBs are weakened by the ingress of liquid metals leading to premature fracture. Zn is a prime embrittler in Fe. Combined STEM and APT measurements (Fig. 2(d)), as well as phase field and DFT calculations revealed that Zn segregates in periodic patterns of large and small excess concentration to ∑5 [001] GBs [8,9]. This pattern is indicative of a miscibility gap of the excess concentration of Zn in the GB and leads to high Zn concentration at the GB even for low bulk concentrations. Here, B and C are elements that can counteract the negative effects of Zn in two ways: they reduce the Zn concentration via a repulsive interaction and increase the GB cohesion and thereby the toughness (Fig. 2(e)).

We demonstrate the intricate interplay between GB chemistry and structure by linking atomistic observations with a thermodynamic description of GB phases and segregation. Our work provides direct links between these atomistic details and macroscopic material behaviour.

References

1. Langenohl, L.; Brink, T.; Freitas, R.; Frolov, T.; Dehm, G.; Liebscher, C.H.: Nat. Commun. 13 (2022) 3331.
2. Ahmad, S.; Brink, T.; Liebscher, C.H.; Dehm, G.: Acta Mater. 268 (2024) 119732.
3. Brink, T.; Langenohl, L.; Bishara, H.; Dehm, G.: Phys. Rev. B 107 (2023) 054103.
4. Langenohl, L.; Brink, T.; Richter, G.; Dehm, G.; Liebscher, C.H.: Phys. Rev. B 107 (2023) 134112.
5. Zhang, S.; Xie, Z.; Keuter, P.; Ahmad, S.; Abdellaoui, L.; Zhou, X., et al.: Nanoscale 14 (2022) 18192.
6. Zhou, X.; Mathews, P.; Berkels, B.; Ahmad, S.; Alhassan, A.S.A.; Keuter, P., et al.: arXiv:2303.09465.
7. Zhou, X.; Ahmadian, A.; Gault, B.; Ophus, C.; Liebscher, C.H.; Dehm, G.; Raabe, D.: Nat. Commun. 14 (2023) 3535.
8. Ahmadian, A.; Scheiber, D.; Zhou, X.; Gault, B.; Romaner, L.; Kamachali, R.D., et al.: Adv. Mater. 35 (2023) 2211796.
9. Darvishi Kamachali, R.; Wallis, T.; Ikeda, Y.; Saikia, U.; Ahmadian, A.; Liebscher, C.H.; Hickel, T.; Maaß, R.: Scr. Mater. 238 (2024) 115758.

Metastable surface phase diagrams

J. Yang[1], N. Peter[2], G. Dehm[2], S. Zhang[3], C. Scheu[3], J. Neugebauer[1], M. Todorova[1]

[1]CM, [2]SN, [3]NG

The knowledge of the thermodynamically stable or metastable phases at the solid surface or solid/water interface is the basis for the rational engineering of interfacial processes. A powerful tool to achieve a detailed understanding of surface thermodynamics is the surface phase diagram. Surface phase diagrams show the stable and metastable surface phases at given environmental conditions such as temperature and chemical potential. Thus, analogous to the use of bulk phase diagrams for engineering material properties in the bulk, surface phase diagrams provide a route to engineer, for example, the catalytic activity of surfaces or to reduce corrosion.

Despite the potential opportunities of engineering surfaces and interfaces using surface phase diagrams, there remain many challenges in constructing them. On the computational side, the large system size and the long simulation times required to model solid/liquid interfaces make such calculations computationally much more expensive than modelling bulk systems. On the experimental side, it is extremely challenging to accurately probe the atomistic structure of an electrochemically active surface. In the present report, we highlight our theoretical developments in constructing surface phase diagrams based on *ab initio* calculations [1,2] as well as experimental characterizations of surface phases in the context of Mg alloy corrosion [3,4].

Within our activities of the Collaborative Research Centre 1394 (see p. 82), we construct the surface phase diagram of a Mg (0001) surface with Ca (Fig. 1a) by combining density functional theory (DFT) calculations and thermodynamic modelling [1]. A major challenge in constructing surface phase diagrams is to correctly include the disordered surface phase, which is beyond the size limitation of present DFT calculations. To overcome this challenge, we fit a cluster expansion (CE) to the DFT-calculated surface energies and are thus able to study the energetics of a much larger surface cell (Fig. 1b). The results clearly show an energy gap between the disordered surface phases and the ordered phase with 1/3 Ca coverage. The resulting surface isotherm shows an order-disorder transition (Fig. 1c). At low temperature and high Ca chemical potential, the stable surface phase is the 1/3 ordered phase; and at high temperature and low Ca chemical potential the disordered phase dominates. This approach proved to be very versatile and has also been successfully applied to the solid/liquid interface in combination with the implicit solvent method, the accuracy of which has been verified by comparison with *ab initio* molecular dynamics calculations [2].

By comparing the predicted surface phase diagrams of Mg-Ca and Mg-Al, we were able to show that Ca preferentially segregates to the top surface of Mg and gets easily dissolved in water, while Al remains in the subsurface region. To better understand the surface phases formed during the corrosion of Mg alloys, we characterize the native oxide formed on the (0001) plane of the Mg alloy Mg-2Al-0.1Ca by combining scanning transmission electron microscopy (STEM) and atom probe tomography (APT) [3]. The annular bright field STEM measurement shows the growth of a (111) MgO oxide layer (Fig. 2a). The APT data further reveals that in the region between bulk Mg and the native oxide, Al is enriched up to ~20 at% (Fig. 2 b, c). The observed Al enrichment is consistent with the inward growth of the native oxide, during which Al substitutions are pushed deeper into the bulk, forming the enriched region at the bulk/native oxide interface.

In addition to the Mg matrix, we study the corrosion of the C15 Al_2Ca Laves phase, which forms as secondary phase particles in Mg-Al-Ca alloys [4]. There has been an ongoing discussion as to whether crystal defects, such as

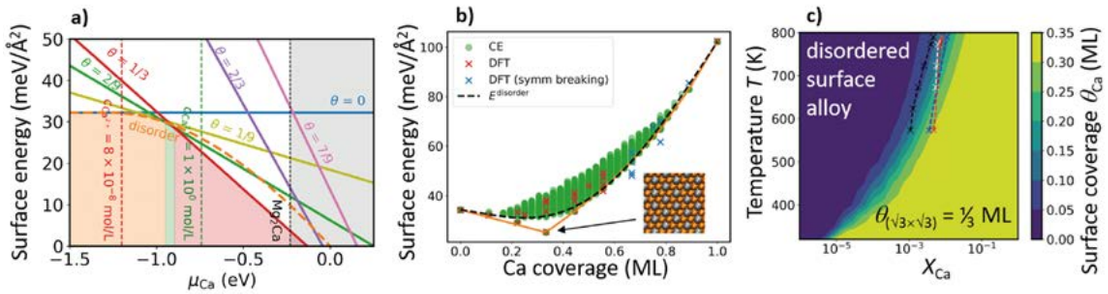

Fig. 1: *Ca substitution on the Mg(0001) surface. (a) Surface phase diagram for the surface in aqueous environment. (b) Surface energies for various Ca coverages and configurations obtained using a DFT based cluster expansion. (c) Heat map depicting coverages achievable at different temperatures T and Ca concentrations X_{Ca} in Mg bulk. Data taken from our work [1,2].*

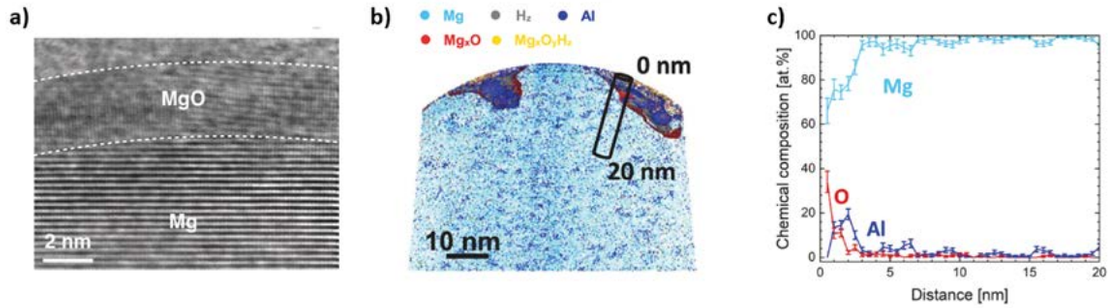

Fig. 2: *Characterization of the native oxide scale on the Mg alloy $Mg_2Al_{0.1}Ca$. (a) Angular bright-field STEM image of the apex of the cleaned atom probe specimen. (b) 3D atom map of the specimen from APT. (c) 1D concentration profile of the cylindrical region indicated in (b) for Mg, Al and O. Data set taken from our manuscript [3].*

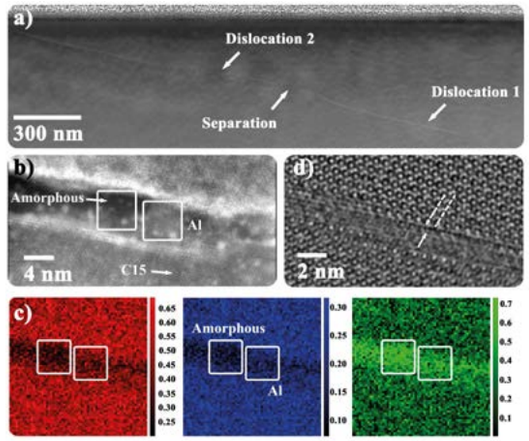

Fig. 3: *Characterization of oxygen enrichment induced changes at the (sub)surface dislocations. Two dislocations have been identified in the HAADF-STEM micrograph in (a). Dislocation 2 shows a distinct structural arrangement in its oxygen-enriched region (b) with amorphous regions coexisting with simple fcc (A1) crystalline regions. Chemical analysis of this exact region by quantitative STEM-EDS spectral imaging analysis (c) shows that the amorphous region has a molar composition close to Al_2O_3 (colour scale in molar fraction), while the crystalline part is close to the Al_2Ca composition. Dislocation 1, in contrast to dislocation 2, is only disordered for a few atomic unit cells, as seen in the HAADF-STEM micrograph in (d). Data taken from own publication [4].*

dislocations and twin boundaries, provide a fast diffusion pathway for oxygen species in alloys and intermetallic materials. However, it is difficult to study this phenomenon in Al-containing intermetallic materials due to the rapid formation of a passivating oxide. We focused on the structural changes at dislocations and twin boundaries during corrosion by combining STEM high-angle annular dark-field (HAADF) micrographs and quantitative STEM energy-dispersive X-ray spectroscopy (EDS) spectral imaging (Fig. 3). We observe that the twin boundary and the dislocation transform into a few nanometres wide amorphous phase, which are depleted in Al and Ca but are highly enriched in oxygen. In the case of dislocations, we additionally observe the coexistence of the amorphous phase with a simple Al-rich A1 fcc phase (Fig. 3b). This A1 phase, which is coherent with the C15 matrix, is only depleted in Ca, not in Al, and is enriched in oxygen. Electron energy-loss spectroscopy revealed the amorphous phase to be Al_2O_3. We thereby show as one of the first studies of its kind, that oxygen diffusion along crystal defects, especially also at the twin boundary, can induce the formation of an amorphous oxide along itself [4].

In conclusion, by combining theoretical calculations and advanced atomic-scale characterization, we demonstrate the existence of complex phase formation and transformation processes at the alloy surface during corrosion. A surface phase diagram provides a powerful tool for understanding surface thermodynamics, as it predicts the stable and metastable surface phases at given thermodynamic conditions. Experiments reveal that partially buried defects such as dislocation and twin boundaries can also undergo chemically induced structural transitions. Understanding these defect phases serves as the basis for further surface engineering for tailored properties, for example, corrosion resistance. Further work is being carried out to exploit the potential of surface phase diagrams in the context of Mg and Ni alloy corrosion within the second phase of the Collaborative Research Centre 1394 (see p. 82).

References

1. Yang, J.; Kumar, K.B.S.; Todorova, M.; Neugebauer, J.: Phys. Rev. Mater. 7 (2023) 095802 .
2. Yang, J.; Todorova, M.; Neugebauer, J.: J. Chem. Phys. 160 (2024) 164715 .
3. Neuß, D.; McCarroll, I.E.; Zhang, S.; Woods, E.; Delis, W.J.; Tanure, L.; Springer, H.; Sandlöbes, S.; Yang, J.; Todorova, M.; Zander, D.; Scheu, C.; Schneider, J. M.; Hans, M.: Corros. Sci. 227 (2024) 111776 .
4. Peter, N.J.; Zander, D.; Cao, X.; Tian, C.; Zhang, S.; Du, K.; Scheu, C.; Dehm, G.: J. Alloys Compd. 936 (2023) 168296 .

Atomic-scale understanding of hydrogen embrittlement and corrosive processes in Al-alloys

H. Zhao[1], P. Chakraborty[2], A. Mingers[3], A. Tehranchi[2], M. López Freixes[1], T. Hickel[2], D. Ponge[1], B. Gault[1], J. Neugebauer[2], M. Rohwerder[3], D. Raabe[1]

[1]MA, [2]CM, [3]GO

High-strength 7xxx Al-alloys, strengthened by Zn- and Mg- rich nanoscale precipitates are widely used in the aerospace industry, and are increasingly used to reduce the weight and fuel consumption of automobiles. As such they are expected to play a key role in reducing CO_2 emissions in the coming decades. As most high-strength metallic alloys, they are highly susceptible to hydrogen embrittlement (HE), often related to stress-corrosion cracking (SCC) leading to intergranular cracking. The alloys' sensitivity to HE and SCC depends on temper and exposure conditions. HE and SCC mechanisms not being fully determined, it remains challenging to define efficient counteracting strategies while maintaining an appropriate property balance.

We initiated a study of the distribution of H in a model alloy. Site specific, isotope labelled atom probe tomography (APT) analyses were performed in samples charged with deuterium [1]. We revealed trapping of H in intermetallic precipitates, and along grain boundaries, where Mg was also segregated (see p. 55). Using these insights, detailed density-functional theory calculations were performed of the evolution of the segregation energies for H across various sites at a model high grain boundary, in conjunction with Mg segregation, Fig. 1.

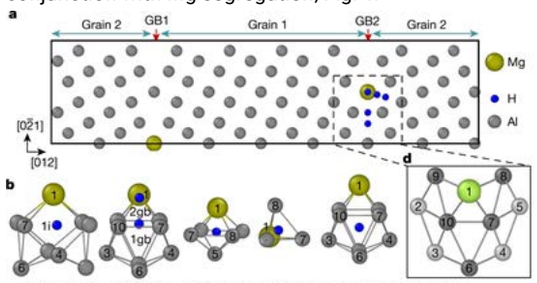

Fig. 1: ***a*** *Schematic representation of the symmetric Σ5 (210) GB in Al shown with two GB planes.* ***b*** *The projected and perspective views of deltahedral packing units show the H adsorption sites of the calculations. Site number 1 is the substitutional site for a Mg atom nearby the H sites located inside the polyhedral packing units (from [1]).*

Separately, H and Mg have a limited influence on the cohesive energy of the grain boundary, which accounts for the difference between the grain boundary and the separation into two free surfaces. However, when H and Mg are co-segregated to the grain boundary, their combination leads to a substantial drop in the cohesive energy, as H is a more potent stabiliser of the free surface. This explains why H facilitates the decohesion of Mg-segregated grain boundaries. Our unique approach combining atomistic-scale experiments and theory helped rationalise the mechanisms leading to hydrogen embrittlement.

In a later study of the aqueous corrosion of the same alloy, we could reveal the kinetic of dissolution of the solutes through scanning flow cell experiments. Using isotopically-labelled APT, we evidenced integration of hydrogen into a nanocrystalline thin oxide layer, enriched in Al, Mg and D, Fig. 2, whereas the other solutes are found segregated to the metal-oxide interface. We reported also a dependence on the alloy's temper state, along with an unexpected tendency for dissolution of the precipitates in the near-surface region, associated to the integration of solutes into the growing oxide. It is crucial to understand these processes to define strategies to mitigate corrosion, that limits lifetime and impacts the sustainability of the alloy.

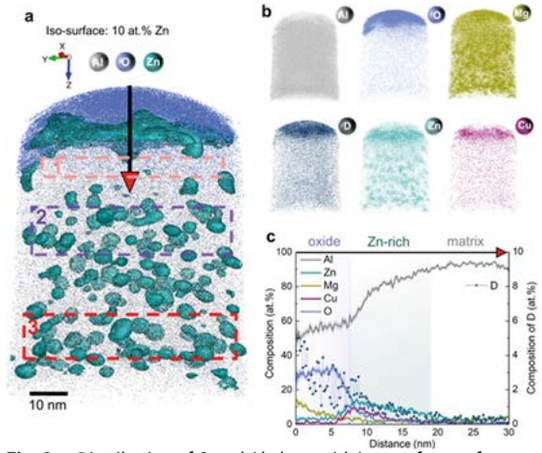

Fig. 2: ***a*** *Distribution of O and Al along with iso-surfaces of 10 at.% Zn highlighting the precipitates.* ***b*** *Atom maps of Al, O, Mg, D, Zn, and Cu.* ***c*** *One-dimensional composition analysis across the oxide (from [2]).*

To confirm the relevance of these observations on a model system to more complex, industrial alloys, we investigated a range of 7XXX-alloys in the form of thick plates processed by industrial partners (7651, 7140). These alloys were studied after SCC tests performed according to ASTM standards, with or without addition of an NaCl solution. The tests were interrupted in order to perform analyses in the region near the progressing intergranular crack. In these alloys, similar processes were revealed [3, 4]. First, in the subsurface region as well as several microns ahead of the moving crack, which we attributed to the corrosion of the fresh surface triggering solute redistribution, i.e. the Mg-rich oxide consumes the locally

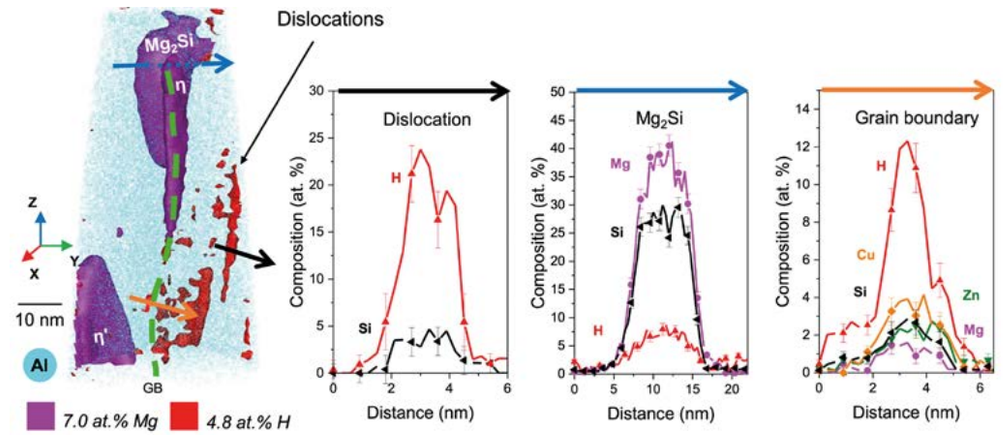

Fig. 3: *APT analysis 4 µm ahead of the intergranular crack showing the presence of dislocations enriched with H and Si. 1D Composition profiles across a dislocation, the Mg_2Si grain boundary intermetallic, and the grain boundary measured along the coloured arrows.*

available Mg, which in turn creates a flux of Mg, along the GB, and in the matrix, destabilising the local equilibria and leading to the dissolution of the strengthening precipitates. Second, H, generated by the splitting of water at the crack tip, is found segregated to grain boundaries and dislocations in the vicinity and several microns ahead of the crack, indicating relatively long range movement of defects and H. These moving dislocation along with local strain may also assist with precipitate dissolution [5].

The very high H content at dislocations suggests possible formation of defect phases. Some of these results were hence also correlated with *ab initio* and atomistic simulations to demonstrate an enhancement in the probability of hydride formation at the crack tips. The *ab initio* simulations show that the most stable Al-based hydride is AlH_3, however this hydride is not stable at room temperature and its formation requires a high hydrogen chemical potential. Interestingly, the defects in the material can assist the formation of it due to their negative pressure field. Fig. 4 depicts the process of the formation of nano-hydrides at the crack tip region in Al using combined molecular dynamics-Monte Carlo (MD-MC) simulations. The loading is intentionally kept below the critical stress intensity factor for cleavage and emission of the dislocations from crack tip.

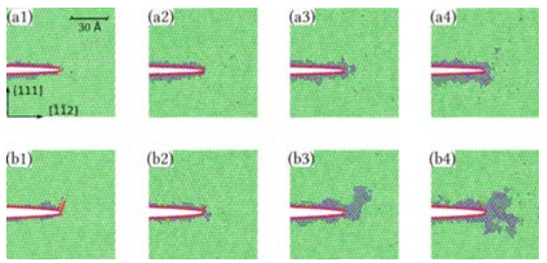

Fig. 4: *Atomic structure of the crack tip regions at T=300 K, at (a) K_I=0.20MPa√m and (b) K_I=0.30MPa√m. The green, red, and purple spheres denote the fcc-Al, non-fcc Al, and H atoms, respectively. In each row the chemical potential of H with respect to its value at Al tetrahedral site is increased from -0.245 eV to -0.185 eV from left to right.*

It is evident that with increasing both the chemical potential of hydrogen and the crack tip loading the formation of nano-hydrides is enhanced. This means that the crack tip region can act as a nucleation region for hydrides due to its negative pressure field. This effect was supported by APT analyses in the region very near to the crack tip in which a high concentration of hydrogen was found [6], particularly near crystalline defects.

In addition to these studies on Al and its alloys, there was for instance a joint study between DFT and APT of hydrides formation in Zircaloy-4 [7,8]. We focused on the detailed mechanism of the redistribution of Sn, a major alloying element in this system, and particularly its segregation to defects formed during the growth of the hydride to accommodate the difference in lattice parameter between the two phases.

References

1. Zhao , H.; Chakraborty, P.; Ponge, D.; Hickel, T.; Sun, B.; Wu, C.H.; Gault, B.; Raabe, D.: Nature 602 (2022) 437.
2. Zhao, H.; Yin, Y.; Wu, Y.; Zhang, S.; Mingers, A.M.; Ponge, D.; Gault, B.; Rohwerder, Michael; Raabe, D.: Nat. Comm. 15 (2024) 561.
3. López Freixes, M.; Zhou, X.; Zhao, H.; Godin, H.; Peguet, L.; Warner, T.; Gault, B.: Nat. Comm. 13 (2022) 4290.
4. López Freixes, M.; Peguet, L.; Warner, T.; Gault, B.: Corros. Sci. 229 (2024) 111904.
5. López Freixes, M.; Zhou, X.; Aymerich-Armengol, R.; Vega-Paredes, M.; Peguet, L.; Warner, T.; Gault, B.: Scripta Mat. 237 (2023) 115690.
6. Tehranchi , A.; Chakraborty, P.; López Freixes, M.; McEniry, E.J.; Gault, B.; Hickel, T.; Neugebauer, J.: Phys. Rev. Materials 7 (2023) 105401.
7. Mouton , I.; Chang, Y.; Chakraborty, P.; Wang, S.; Stephenson, L.T.; Britton, T.B.; Gault, B.: Materialia 15 (2021) 101006.
8. Chakraborty , P.; Mouton, I.; Gault,B; Tehranchi, A; Hickel, T; Neugebauer, J; Phys. Rev. Materials 8 (2024) 033605.

Microstructure and mechanics of ice

J.P. Best[1], R. Dubosq[2], B. Gault[2], C. Liu[2], S. Motahari[2], R. Ramachandramoorthy[1], T.M. Schwarz[2], T. Sinani[1], E.V. Woods[2]

[1]SN, [2]MA

From 2011 to 2014, satellite data revealed a negative mass balance of -269 ± 51 Gt/year in glaciers like Kangerdlugssuaq and Upernavik Isstrøm, attributed to calving and crack promotion [1]. The formation of crevasses in Greenland and Antarctica is mainly driven by the brittle failure of ice at low strain rates, influenced by microstructural heterogeneity and anisotropic elastoplastic deformation. Consequently, developing simulation and experimental protocols to analyse the mechanical response of ice and its microstructure is imperative. Despite its importance, the complex nature of ice presents substantial challenges in both simulation and experimental testing, particularly on small scales, precluding the study of fundamental mechanisms and leaving open questions as to how natural ice deforms.

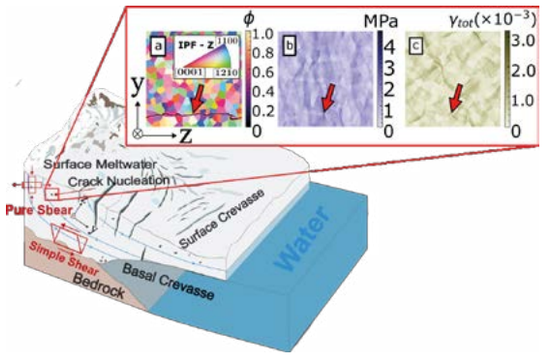

Fig. 1: *Marine-terminating glacier with a floating ice shelf, featuring both large surface and basal crevasses. Blue lines with arrows on the glacier's cross-section indicate the direction of ice movement. The inset figures show the microstructure of ice with a random texture, undergoing uniaxial tensile stress along the y-axis (crack pattern (a), distribution of tensile von Mises stresses (b), and plastic shear (c) in ice). The red arrows mark the crack nucleation site.*

In the realm of simulation, microstructure-sensitive modelling has been pivotal. Our research has led to the development of a microstructure-sensitive crystal plasticity and phase-field model to study plastic deformation, damage initiation, and propagation under various strain rates in hexagonal open-packed polycrystalline ice, the predominant phase on Earth (see Fig. 1). By using Bayesian optimisation, we derived material parameters for the micromechanical model from experimental results, such as electron backscatter diffraction and indentation experiments. The modelling results indicate that the activation of basal dislocations results in a brittle-to-ductile transition in ice at a low strain rate of 10^{-7} s^{-1} under tension. At higher strain rates, the intrinsic plastic anisotropy of ice causes heterogeneous deformation among grains and stress concentration near grain boundaries, leading to crack initiation and increased brittleness. Under compression, cracks typically do not propagate throughout the specimen due to a significant decrease in stress around the crack tip upon propagation. Additionally, shear-induced basal texture at the bottom of ice layers and along glacier valley sides exacerbates the intrinsic brittleness of ice. This study provides crucial insights into the micromechanical deformation and fracture mechanisms of ice, elucidating the intricate process of crevasse development in polar ice sheets.

To complement these modelling efforts, local chemical analyses have been employed to study the structure and chemistry at local scales. Recent advancements have enabled the analysis of frozen liquids and soft materials by atom probe tomography (APT), facilitating the examination of solute distribution in their native environment [2]. This includes cryogenic protocols for APT specimen preparation from bulk frozen water [3] and various aqueous and organic solutions [4]. While it is known that solutes alter the properties of ice, their distribution in natural ice and segregation at defects like grain boundaries remain poorly understood. Electron microscopy has shown potential in analysing ice in both amorphous and crystalline states, but ice's sensitivity to irradiation by electrons and X-ray limits the application of spectroscopic techniques for solute distribution analysis. Future plans include investigating natural ice using APT, which will provide further insights into the impact of solutes on ice properties.

Another significant area of our research is to develop correlative *in situ* nanomechanics workflows, which link microstructural descriptions of ice deformation with local analyses by APT. A low-temperature nanoindentation setup featuring Peltier coolers has been developed to examine real-time ice deformation within our environmental scanning electron microscope (E-SEM). This innovative system offers precise temperature control, enabling direct microscale investigations into ice mechanics *in situ* [5]. Given that grain boundaries serve as interfaces where soluble impurities tend to segregate, understanding how these impurities affect fracture at grain boundaries is crucial. These insights can significantly enhance models of glacier flow in natural environments. Ice samples with varying cooling rates, which affect grain size and gas bubble frequency, and impurity concentrations are being prepared to correlate fracture with grain boundary chemistry, determined using APT.

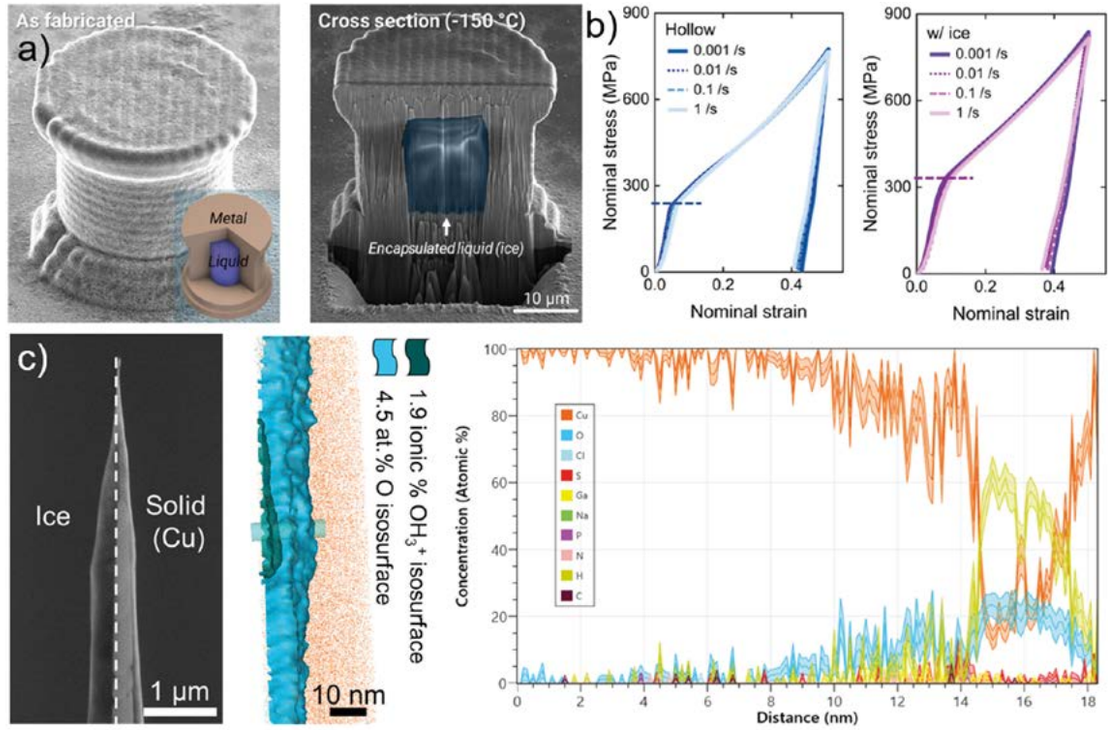

Fig. 2: *Copper microcylinders with encapsulated liquid frozen at -150°C and cross-sectioned using focussed ion beam (a). Stress-strain response of hollow copper microcylinders and with ice compressed at different strain rates (b). APT analysis of ice and copper interface (c).*

A recent development in our research is localised electrodeposition in liquid (LEL), an additive microfabrication technique that operates in a liquid environment consisting of a weak acid-based supporting conductive electrolyte (see p. 72). Utilising this liquid fabrication environment, we have developed a novel methodology to encapsulate the supporting electrolyte within microscale 3D metal microarchitectures. The LEL technique's sub-micron printing precision enables the encapsulation of pico-litre volumes of supporting conductive electrolyte within metal microvessels in a single step. This capability allows the creation of liquid-encapsulated 3D microarchitectures, where the liquid can potentially influence the mechanical response of the entire structure. The encapsulated liquid within the metallic material can alter its mechanical properties, exhibiting diverse behaviours due to phase changes under various temperature conditions (Fig. 2a). Our research focuses on the impact of encapsulated liquid on the rate- and temperature-dependent mechanical properties of metal-liquid microvessels and their interactions. *In situ* mechanical tests in both compression and tension have been conducted at various temperatures and strain rates to systematically study these effects inside an SEM (Fig. 2b). Comparing the mechanical properties of liquid-encapsulated structures with hollow metal structures helps elucidate the influence of the encapsulated liquid and ice on overall structural properties.

Another area of application is the analysis of liquid-solid interfaces, which pose a major challenge for analytical techniques. However, processes taking place at reactive interfaces are crucial for a wide range of applications such as catalysts, batteries, corrosion and biology. With these newly developed protocols, it has been shown that it is possible to prepare specimens with liquid-solid interfaces (Fig. 2c), also allowing the study of early-stage corrosion of a Mg-alloy quasi *in situ* [6]. Such approaches, among other benefits, will help rationalise the mechanisms controlling the corrosion of biodegradable alloys.

References

1. Benn, D.I.; Cowton, T.; Todd, J.; Luckman, A.: Current Climate Change Reports 3 (2017) 282.
2. El-Zoka, A.A.; Stephenson, L.T.; Kim, S.-H.; Gault, B.; Raabe, D.: Adv. Sci. 10 (2023) 2300626.
3. Woods, E.V.; Singh, M.P.; Kim, S.-H.; Schwarz, T.M.; Douglas, J.O.; El-Zoka, A.A.; Giulani, F.; Gault, B.: Microsc. Microanal. 29 (2023) 1992.
4. Singh, M.P.; Woods, E.V.; Kim, S.-H.; Jung, C.; Aota, L.S.; Gault, B.: Batteries & Supercaps 7 (2024) e202300403.
5. Dubosq, R.; Woods, E.V.; Gault, B.; Best, J.P.: PLoS ONE 18 (2023) e0281703.
6. Schwarz, T.M.; Yang, J.; Aota, L.S.; Woods, E.V.; Zhou, X.; Neugebauer, J.; Todorova, M.; McCarroll, I.; Gault B.; Adv. Mater. 36 (2024) 2401735.

Construction of defect phase diagrams and metastable defect phase diagrams

A. Tehranchi[1], S. Zhang[2], P. Mathews[1], S. Ahmad[3], X. Zhou[4], G. Dehm[3], C. Scheu[2], T. Hickel[1], J. Neugebauer[1]

[1]CM, [2]NG, [3]SN, [4]MA

The properties of a material depend on both its bulk phase distribution and its defects. It is conventionally believed that the former is determined by thermodynamic equilibrium described by phase diagrams whereas the latter originates through non-equilibrium processes. However, the recent advances in experimental characterization techniques with atomic resolution of defects embedded in bulk – worldwide and at MPI-SusMat – challenge this conventional separation [1]. The striking finding that defect formation can be controlled by thermodynamic parameters opens exciting routes for inducing and controlling defect formation, ultimately providing materials researchers with a tool to tailor microstructure morphology. However, to harness this mechanism effectively across a wide range of material systems, it is essential to have a computational approach that goes well beyond conventional phase diagrams by including also thermodynamically (meta-)stable defect phases.

For *ab initio* simulations as performed in the CM department, their high computational costs allow only the calculation of small system sizes consisting of a few hundred atoms. These sizes are far too small to simulate the whole closed system. Instead, the various subsystems such as point defects/solutes in the bulk, the different defect types such as surfaces, grain boundaries, etc. are computed separately. The calculations of small-sized defects represent thermodynamically open systems that can have vastly different compositions than the surrounding host matrix. For such thermodynamically open systems, we use the grand potential $\Omega(T,P,\mu_\alpha)$ of defects as a replacement of the Gibbs energy which is the key quantity defining bulk phase diagrams. It can be computed as:

$$\Omega(T=0,P=0,\mu_{solute}) = E^{\sigma}_{tot} - E^{bulk}_{tot} - n_{solute}\mu_{solute}$$

where $E^{\sigma}_{tot}, E^{bulk}_{tot}$ are total energies of supercells with and without a defect state σ, and n_{solute}, μ_{solute} are the number of solute atoms in the defect and their chemical potential. The calculations are done at zero temperature, T, and zero pressure, P.

We use the chemical potential to tune the defect state of the material against precipitate formation. Practically this is achieved by driving the solute concentration beyond the solubility limit, i.e., to go into supersaturation. We exploited the notion that an intrinsic and ab initio accessible upper limit of μ_{solute} for achievable supersaturation is the formation of coherent precipitates in the host matrix at $\mu_{coherent}$.These coherent precipitates are metastable with respect to thermodynamically stable and plastically fully relaxed precipitates formed at $\mu_{equil.}$, setting the intrinsic lower limit for supersaturation.

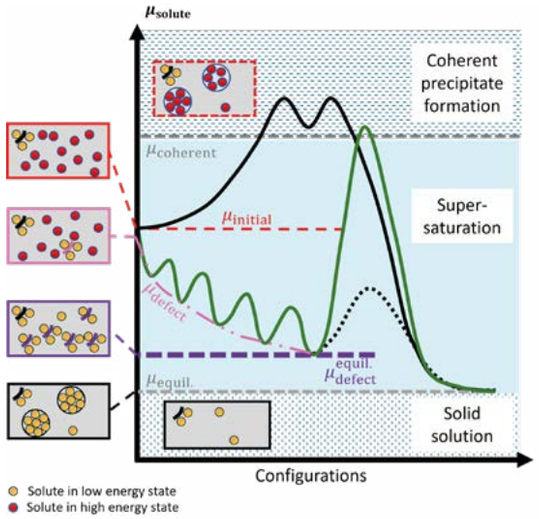

Fig. 1: *Possible reaction pathways starting from a supersaturated solid solution [2].*

The interesting region (marked cyan in Fig. 1) is where homogeneous nucleation via coherent precipitate formation is energetically impossible. In addition, by increasing μ_{solute} such that the grand potential becomes negative, one can controllably induce high defect concentrations. The lower limit of this region is the chemical potential $\mu^{defect}_{equil.}$ at which the defects are in thermodynamic equilibrium with the surrounding host matrix, i.e. once a higher chemical potential has dropped to this value, defect formation stops. The complete reaction path leading to defect formation is shown by the green line in Fig 1. Starting from a supersaturated solid solution with a chemical potential of $\mu_{initial}$, solute-driven defect formation occurs. Since defect formation is fuelled by solute removal from the matrix, the solute concentration in the matrix, and thus the solute chemical potential, decreases as defect formation proceeds until the energy gain from defect formation becomes too low to overcome the defect nucleation barrier. To build up defect phase diagrams as a toolbox for materials design, the biggest challenge is to identify various thermodynamic phases of individual defects under investigation.

On the experimental side, we have developed a quasi in situ approach to observe phase transformation of a single grain boundary (GB) using scanning transmission electron microscopy (STEM) at atomic resolution. Firstly, a focused ion beam (FIB) STEM sample was taken from a textured Mg thin film to locate special GBs [3], such as the symmetric Σ7 [0001] (3,-1,-2,0) tilt GB (Σ7 in short). By using a Xe-plasma FIB, the STEM sample was prepared free of Ga contamination [4].

After imaging the Ga-free Σ7 GB at atomic resolution (Fig. 2a), the STEM sample was put back to a Ga-source FIB in order to intentionally introduce Ga to the imaged area. As shown in Fig. 2b, the GB underwent a structural transfor-mation, as the tetrahedron structural units (filled in green) was progressively replaced by capped trigonal prisms (filled in red), as Ga was increasingly sputtered onto the sample. As the local Ga concentration (c_{Ga}) rises as well as the chemical potential (μ_{Ga}), chemical ordering appeared at the GB, as bright atomic columns in Fig. 2c,d indicate the sites with Ga segregation.

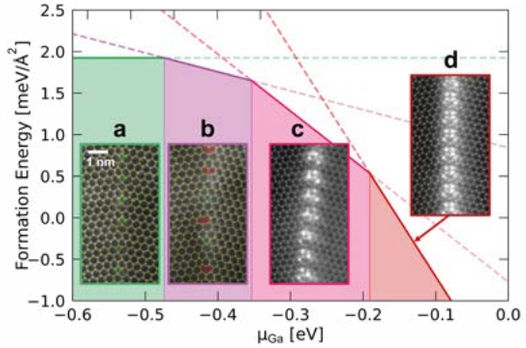

Fig. 2: *Construction of a defect phase diagram from observed phase transformations. The calculated Mg Σ7 GB phase diagram using DFT and experimentally-observed GB structures. The bottom axis μ_{Ga} is the chemical potential of Ga with respect to the bulk Ga phase. (a) GB of pure Mg has T-type structure units; (b) GB with Mg segregation has A-type structure units; (c-d) ordering of Ga atoms with (c) 3 and (d) 6 columns of Ga in each structural unit [4].*

The experimental approach to trigger and observe phase transformations between individual defects opens a way to investigate their thermodynamic stability for the construction of defect phase diagrams. As explained above (Fig. 1), we use the chemical potentials (in this case μ_{Ga}) among the thermodynamic variables to describe the defect-containing ensemble, instead of the chemical compositions. This description circumvents the difficulty to define a local composition of solutes at the defect. In equilibrium, the chemical potentials are equal among different defects and their adjacent bulk phases.

The experimentally observed Σ7 GB has two known defect phases, the A-type (capped trigonal prism unit seen with Ga segregation) and the T-type (tetrahedron unit, seen for pure Mg GB). The stability of these defect phases has been studied by constructing the defect phase diagram using ab initio simulations. For this, density functional theory (DFT) calculations are performed on supercells containing the Σ7 GB with the Ga atom arrangements seen in the different defect phases. The formation energies for these defect phases are calculated using Eq. 1 (and normalized by the GB area of cross-section) and are plotted against the chemical potential μ_{Ga} (Fig. 2). The different slopes of the formation energies are due to the number n_{Ga} of Ga atoms at the GB.

The T-type is energetically more stable than the A-type for the case of the pure Mg GB and is stable at very low chemical potentials in the defect phase diagram. Ga being an A-type stabilizer, segregates and transforms the GB to the A-type. With more Ga atoms at the GB, the GB structural unit does not change. μ_{Ga} = 0 eV represents the chemical potential of Ga in its bulk, hence, the 6-Ga configuration is stable at a comparatively higher chemical potential and is metastable. The driving force of reduction of the solute chemical potential leads to a preference for defect phases at lower chemical potentials, and the relevant range can be determined using the Ga concentration.

Similarly, various defects can be studied using defect phase diagrams, also directly by ab initio simulations, based on which experiments can be devised. Furthermore, defect phase diagrams for individual defects can be linked with microstructure-property diagrams to identify desired defect phases to induce certain properties in the alloys as done within the Collaborative Research Centre 1394 (see p.82) where we contribute from atomic-scale structural characterization and modelling. Considering the kinetic barriers for precipitation will open an additional playground to design defect states of materials. This will allow us to tailor experiments in such a way that certain defects are inserted into the alloy. Therefore, (metastable) defect phase diagrams are roadmaps for materials design which consider not only bulk phases but also defects, including stable and metastable defect phases, thereby offering a novel way for designing tailored materials.

References

1. Zhou, X.; Ahmadian, A.; Gault, B.; Ophus, C.; Liebscher, C.; Dehm, G.; Raabe, D.; Nature Commun. 14 (2023).
2. Tehranchi, A.; Zhang, S.; Zendegani, A.; Scheu, C.; Hickel, T.; Neugebauer, J.: Acta Mater 277 (2024) 120145.
3. Zhang, S.; Xie, Z.; Keuter, P.; Ahmad, S.; Abdellaoui, L.; Zhou, X.; Cautaerts, N.; Breitbach, B.; Aliramaji, S.; Korte-Kerzel, S.; Hans, M.; Schneider, J.M.; Scheu, C.: Nanoscale 14 (2022) 18192.
4. Zhou, X.; Mathews, P.; Berkels, B.; Ahmad, S.; Alhassan, A.S.A.; Keuter, P.; Schneider, J.M.; Raabe, D.; Neugebauer, J.; Dehm, G.Hickel, T.; Scheu, C.; Zhang, S.: arXiv:2303.09465.

Fracture across scales

M. Mrovec[1], R. Drautz[1], E. Bitzek[2], J.P. Best[3], Y. Hu[4], F. Roters[4]

[1]ICAMS, [2]CM, [3]SN, [4]MA

Enhancing the longevity of structures is a major strategy for improving the sustainable use of materials. Therefore, understanding and controlling fracture is a key interdepartmental research activity at MPI-SusMat. Furthermore, the ability to accurately predict the onset of fracture, be it by overloading, fatigue, high-temperature creep, environmental effects, or combinations thereof, allows for reducing the amount of material required for structural integrity (i.e., lightweighting) and thus has an additional impact on sustainability.

At the core, fracture corresponds to cleavage of atomic bonds. Atomistic simulations, therefore, can provide crucial information about the energetics of cracks and other defects, as well as on the processes involved during fracture. Due to the long-range stress field of cracks, it is necessary to study large systems containing at least many thousands of atoms to be able to neglect boundary effects. At the same time, it is essential to employ a model describing interatomic interactions that are not only efficient but also highly transferable to reliably capture bond breaking under non-equilibrium conditions.

The recent advent of machine-learned (ML) interatomic potentials has revolutionized the field of atomistic modelling, and many new approaches have been advanced in the past years. The group of R. Drautz developed several interatomic potentials based on the atomic cluster expansion (ACE). These potentials deliver accuracy approaching that of quantum mechanical methods while remaining computationally efficient. In our simulations of crack propagation in diamond (Fig. 1), we demonstrated that ACE could correctly reproduce the brittle fracture of diamond, unlike most other classical and ML potentials [1]. The high transferability of ACE potentials was also recently demonstrated in the study of grain boundary fracture of different fcc metals, highlighting the unusual brittle fracture of iridium.

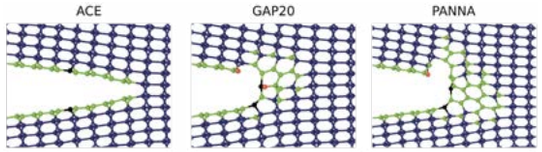

Fig. 1: *Crack tip configurations in diamond as predicted by different ML potentials [1]. Only the ACE potential leads to the correct result.*

Together with the *Microstructure and Mechanics* group of E. Bitzek, an ACE potential for tungsten was developed that could reproduce the crack-tip reconstruction observed in density functional theory calculations. Using this potential in large-scale simulations of blunted crack tips showed that given the additional degrees of freedom at the curved crack tip surface, bcc metals could undergo a local phase transformation at the crack tip. This observation could explain observed differences between experiments with blunt precracks and simulations with idealized, atomically sharp cracks. Crack tip plasticity in W has also been extensively studied in the ERC project microKIc (see p. 56). Due to the comparatively large scales achievable with semi-empiric potentials (hundreds of millions of atoms), these simulations can be particularly useful for interpreting nano- and micromechanical fracture tests as performed in the *Mechanics at Chemical Interfaces* group of J.P. Best.

His group's research highlights the critical role of temperature and impurity segregation in determining fracture toughness and deformation behaviour at local scales, thereby paving the way for improved material design in high-temperature applications. One key material under investigation is tungsten, a prime candidate for plasma-facing applications in fusion reactors due to its high-temperature resilience and ability to withstand intensive particle fluxes. However, operational heat flux can recrystallize tungsten's initial microstructure, increasing its brittle-to-ductile transition (BDT) temperature. A significant study employed microcantilever testing and local chemical analysis via atom probe tomography to investigate the impact of impurity segregation on the fracture toughness of high-purity recrystallised tungsten [2]. The results showed brittle failure at high-angle grain boundaries, with fracture toughness significantly lower than that of the cleavage plane in tungsten microcantilevers. Phosphorous segregation at grain boundaries was identified as a key factor in embrittlement, a conclusion supported by atomistic simulations, which also revealed mechanisms of crack-grain boundary interactions that depend on phosphorous segregation (Fig. 2).

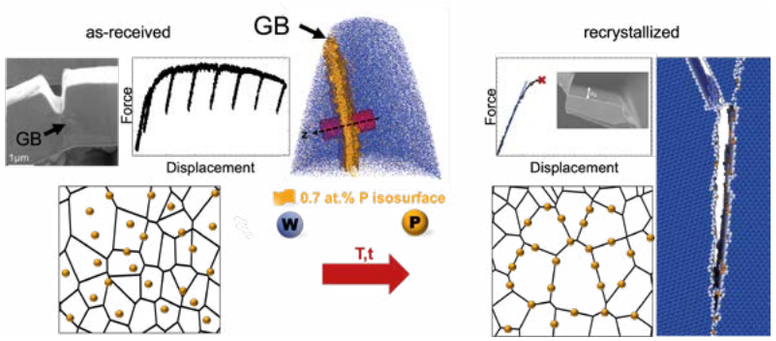

Fig. 2: *P-segregation to grain boundaries at high temperatures leads to embrittlement even in 99.98 at.%. pure tungsten [2].*

The fracture toughness of the cubic *C*15 $CaAl_2$ Laves phase, an intermetallic precipitate critical for enhancing Al and Mg alloys, was also examined using nano- and micromechanical approaches [3]. Correlative nanoindentation and electron channelling contrast imaging indicated that brittle fracture predominantly occurred on {011} planes. Atomistic simulations on a model *C*15 Laves phase showed that this preference of {011} cleavage planes over the more energetically favourable {111} planes is due to the kinetics of bond-breaking controlling the fracture planes in complex crystal structures. Further exploration into the deformation behaviour of the *C*15 $CaAl_2$ Laves phase at elevated temperatures showed a nanoscale brittle-to-ductile transition [4]. *In situ* testing, including nanoindentation and micropillar splitting, identified changes in deformation behaviour correlated with temperature. High-temperature nanoindentation quantified the BDT temperature range, indicating a transition at ~0.55T_m. Micropillar splitting tests showed increased apparent fracture toughness, with crack-free plastic deformation observed above 400 °C. Transmission electron microscopy attributed the BDT of $CaAl_2$ to enhanced dislocation plasticity at higher temperatures. This work on the Laves phase fracture was a central focus of the first phase of SFB 1394 (see p. 82).

Knowing the properties of the precipitates is not sufficient to understand the fracture behaviour of a precipitate-containing alloy. Their volume fraction, morphology, and distribution can critically influence the material's fracture toughness. Therefore, continuum-scale modelling is crucial to obtaining insights into the failure of engineering materials under real-world conditions. Such modelling becomes even more important in the context of sustainability because recycled alloys always contain tramp elements that can lead to the formation of undesired phases. One example is the Fe content in Al scrap, which leads to brittle AlFeSi phases in Al alloys. Here, continuum simulation, for example, can be used to obtain more damage-tolerant microstructures. The underlying models must, however, be capable of capturing different damage mechanisms (brittle for intermetallics, ductile for matrix). The *Theory and Simulation group* of F. Roters developed a unified phase-field model to address both failure modes in one model. An example of its validation is shown in Fig. 3, where standard double-notch simulations are compared with the experiment. An additional benefit is that the unified damage model can be used in conjunction with any continuum-scale plasticity model. Further extension of our damage model is realized by adding a phenomenological, stress-state dependent damage evolution law, which can meet the requirements of our industrial partner, enabling the study of realistic damage behaviour under different loading conditions.

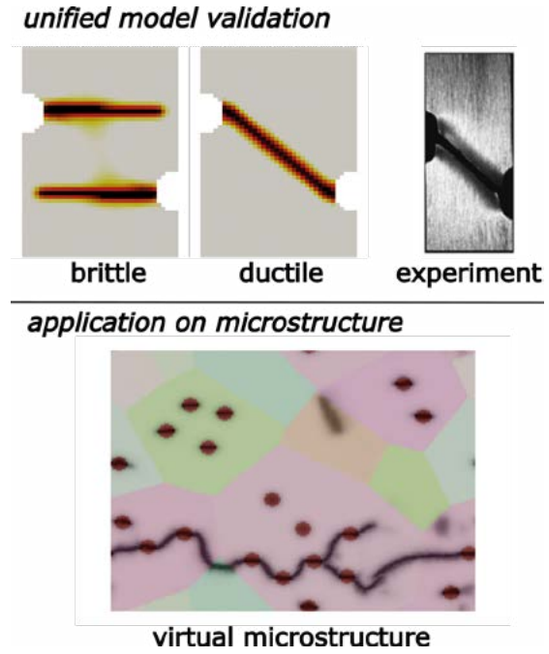

Fig. 3: *Brittle and ductile failure modes are captured with the unified model (top figure). Damage development (annotated with black traces) can be predicted for virtual microstructures (bottom figure).*

Along with the unified damage model and its adaptations mentioned above, we are continuously working on improving our DAMASK software (see p. 78) to address the numerical difficulties that arise in damage simulations. A new spectral solver for the mechanics problem was added to further help users accelerate their analysis.

With its combined expertise in fracture mechanics, plasticity, damage, corrosion, micromechanical testing, and simulations from the electronic to the continuum scale, the MPI-SusMat is uniquely positioned to improve the longevity of materials under realistic usage conditions while reducing the impact of accumulated tramp elements during recycling on the mechanical properties of alloys.

References

1. Qamar, M.; Mrovec, M.; Lysogorskiy, Y.; Bochkarev, A.; Drautz, R.: J. Chem. Theory Comput. 19 (2023) 5151.
2. Tian, C.; Ma, Y., Ghafarollahi, A.; Patil, P.; Dehm, G.; Bitzek, E.; Rasinski, M.; Best, J. P.: Acta Mater. 259 (2023) 119256.
3. Best, J. P.; Kanjilal, A.; Ghafarollahi, A.; Rehman, U.; Tian, C.; Bishara, H.; Bhat, M. K.; Christiansen, L.; Bitzek, E.; Stein, F.; Dehm, G.: J. Mater. Sci. 59 (2024) 12677.
4. Kanjilal, A.; Ahmadian, A.; Freund, M.; Sun, P.L.; Korte-Kerzel, S.; Dehm, G.; Best, J. P.: Materials & Design (2024) 113206.

Chemical ordering effects in complex alloys

S. Waseda[1], T. Hickel[1], S. Ghosh[1], Y. Gong[1], F. Körmann[1], J. Neugebauer[1], B. San[2], G. Dehm[2], Y. Li[3], D. Raabe[3], B. Gault[3]

[1]CM, [2]SN, [3]MA

Chemical ordering can significantly impact materials' properties, so understanding these complex reactions is critical for designing chemically complex alloys. In the last years, we have addressed related experimental and computational challenges for some important materials including the famous Zener ordering, i.e., the carbon-driven ordering in ferrite, TiNbZr with potential hydrogen storage, and enabling characterisation of short-range order (SRO) in high-entropy alloys (see p. 67,89).

The ordering of carbon atoms in ferrite, also known as Zener ordering, is a phenomenon in which carbon atoms occupy the same sublattice depending on the temperature and the carbon content. This phenomenon was first identified by Clarence Zener in the mid-20th century [1] and has since been a crucial topic due to its significant impact on the mechanical properties of steel, the most widely used metallic material worldwide. Zener ordering is considered to be caused by long-range elastic interactions due to the tetragonal distortion stemming from the anisotropic nature of the body-centered cubic (bcc) sublattices [2]. Zener originally formulated this in his mean field method, which provided a foundational theoretical framework.

However, our studies evidence a more complex picture. Repulsive carbon-carbon interactions inhibit the ordering [3], while softening of the elastic constants at higher temperatures promotes it. These contrasting effects lead to a supposed confirmation of Zener's theory, previously tested at low-temperature limits (around 0 K) and high-temperature limits (around the ferrite-austenite transition temperature). Yet, at more pertinent temperatures around ambient temperature, Zener's mean field model deviates significantly from the actual ordering behaviour. This deviation has strong implications for the stability of martensite, a phase critical to the hardness and strength of steel.

Beyond long-range ordering, SRO in multi-component alloys is often hard to quantify experimentally. In high-entropy alloys, the large compositional phase space is also inherently computationally challenging [4]. Experimentally, the occurrence of an upper yield point in some tensile experiments, as well as planar glide in CoCrFeMnNi alloys, was proposed to be associated to SRO. We performed *in situ* and analytical transmission electron microscopy (TEM) studies and confirmed planar glide and dislocation pinning. However, detailed atom probe tomography (APT) and atomic resolved scanning TEM combined with energy-dispersive X-ray spectroscopy (EDS) could not evidence SRO [5]. In the next step, we explored if SRO can

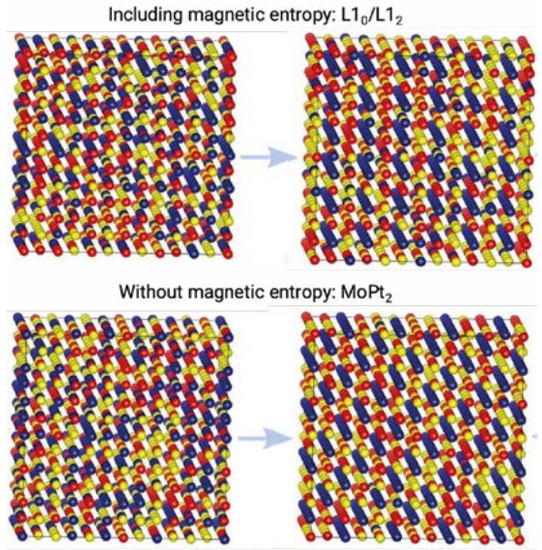

Fig. 1: *Different types of chemical ordering and SRO in CrCoNi as obtained for different treatments of magnetism in the simulations. Left: T=1250 K, right: 950 K. The inclusion of magnetic entropy stabilizes an L12/L10 type of order [9].*

be detected in this multi-element system by scanning TEM-EDS. We computationally generated samples with random occupation of atoms and with some degree of SRO and performed atomic resolved scanning TEM-EDS simulations. Note that the concentration of all elements remained the same for the randomly-configured alloy and the alloy with SRO, and only the species spatial distribution in the 10 nm thin sample were swapped. Interestingly, the results for the model sample with SRO revealed that the composition of the partially ordered element Cr is overestimated by a factor of two in the scanning TEM-EDS signal, whereas that of other elements is slightly underestimated due to the channelling effects on X-ray generation [6]. This indicates that channelling effects may help to detect SRO in thin TEM foils by enhancing the signal in thin foils tilted in zone axis.

Given experimental challenges, *ab initio* computations of SRO are highly desirable. CrCoNi, a prototypical multi-component alloy combining the challenges of magnetism and chemical complexity, is currently the subject of numerous experimental and theoretical efforts to quantify SRO and its possible implications. Initial *ab initio* energy-based lattice Monte Carlo simulations suggested a trend of increased Cr-Co and Cr-Ni neighbours at the expense of Cr–Cr pairs. As a possible ground state ordering, computationally, an alternating pattern of one Cr atomic layer and two mixed Co/Ni atomic layers in the (100) direction has been suggested using the cluster expansion technique [7]. However, using a combination of *ab initio* and more accurate on-lattice machine learning potentials with subsequent canonical Monte Carlo simulations, we found an energetically much more preferable $MoPt_2$-like ordering, characterized by a similar alternation of one layer of Cr atoms and two layers of mixed Co and Ni atoms, but in the (110) direction [8].

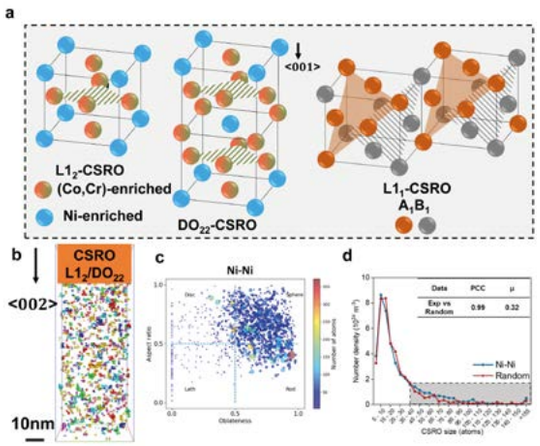

Fig. 2: *Multiple types of chemical SRO domains in 3D in an annealing CoCrNi alloy obtained by proposed machine-learning APT approach. (a) Experimental derived SRO configurations and elemental site occupancies. (b) 3D map of the $L1_2/DO_{22}$ type SROs. (c, d) The corresponding morphology and size distributions [10].*

This $MoPt_2$-type ordering, also found in Cr-Ni binary alloys, has also been reported by neural network potentials in hybrid Monte Carlo/molecular dynamics simulations, in addition to $L1_0$-type clusters. The underlying origin of $L1_0$-type ordering in the computations was unclear, and it was speculated that magnetism may play an important role. We have developed a scheme to incorporate magnetic fluctuations [9] to unravel the possible impact of magnetism. The impact of magnetism on chemical ordering was studied by a combination of *ab initio* simulations, machine learning potentials, and Monte Carlo simulations. Remarkably large magnetic energies are revealed for some mixed $L1_2/L1_0$ type ordered configurations. Our analysis showed that these are rooted in strong nearest-neighbour magnetic exchange interactions and chemical bonding among the constituent elements. It turned out that there is a delicate interplay between magnetism and stability of $MoPt_2$ and $L1_2/L1_0$ type of order, depending on the actual treatment of magnetic fluctuations, which may explain the current opposing experimental and theoretical findings (see Fig. 1).

Going back to APT, the technique has long been expected to enable characterisation of SRO in 3D, but identification of SRO has been hindered by APT's anisotropic spatial resolution and limited detection efficiency. Inspired by the possibilities offered by machine learning methods developed to process complex microscopy and microanalysis data, we put forward a machine-learning enhanced APT approach to quantify the chemical SRO domains in 3D in an annealing CoCrNi alloy followed by furnace cooling [10]. This approach makes full use of the highest-quality, near-atomic resolution of APT in a single dimension, combined with its high elemental analytical ability. As shown in Fig. 2, the $L1_2/DO_{22}$ type SROs were observed in 3D, mainly arising from the Ni-Ni repulsion along the (001) direction. Moreover, we found that there is either Co/Cr/Ni repulsion in the (111) direction, which matches the $L1_1$ type SRO structure. Thus, two distinct different SRO structures were found experimentally. The fruitful quantitative information of these SRO structures, such as their number density, size, and morphology, can be obtained. The occurrence of these SROs led to a 17 % increase in the electrical resistivity.

Efforts are planned in the near future to provide a more general perspective on all these results, which MPI-SusMat is uniquely positioned to provide.

References

1. Zener, C.: Phys. Rev. 74 (1948) 639.
2. Maugis, P.; Connétable, D.; Eyméoud, P.: Scr. Mater. 194 (2021) 113632.
3. Waseda, O.; Morthomas, J.; Ribeiro, F.; Chantrenne, P.; Sinclair, C. W.; Perez, M.: Model. Simul. Mat. Sci. Eng. 27 (2018) 015005.
4. Ferrari, A.; Körmann, F.; Asta, M.; Neugebauer, J.: Nat. Comp. Sci. 3 (2023) 221.
5. Lee, S.; Duarte, M. J.; Feuerbacher, M.; Soler, R.; Kirchlechner, C.; Liebscher, C. H.; Oh, S.H.; Dehm, G.: Mat. Res. Lett. 8 (2020) 216.
6. Utt, D.; Lee, S.; Xing, Y.; Jeong, H.; Stukowski, A.; Oh, S. H.; Dehm, G.; Albe, K.: Nat. Comm. 13 (2022) 4777.
7. Pei, Z.; Gao, M.C.; Stocks, G.M.: npj Comp. Mat. 6 (2020) 122.
8. Ghosh, S.; Sotskov, V.; Shapeev, A.V.; Neugebauer, J.; Körmann, F.: Phys. Rev. Mat. 6 (2022) 113804.
9. Ghosh, S.; Ueltzen, K.; George, J.; Neugebauer, J.; Körmann, F. (2024). DOI: 10.21203/rs.3.rs-3978660/v1.
10. Li, Y.; Colnaghi, T.; Gong, Y.; Zhang, H.; Yu, Y.; Wei, Y.; Gan, B.; Song, M.; Marek, A.; Rampp, M.; Pei, Z.; Wuttig, M.; Ghosh, S.; Körmann, F.; Neugebauer, J.; Wang, Z.; Gault, B.: Adv. Mater. 36 (2024), 2407564.

Nanostructured metals for electrocatalysis

M. Vega-Paredes[1], X. Geng[2], A. Saksena[2], S. Zhang[1], A. Mingers[3], S.H. Yoo[4], M. Todorova[4], J. Neugebauer[4], C. Liebscher[5], K. Tschulik[6], C. Scheu[1], B. Gault[2]

[1]NG, [2]MA, [3]GO, [4]CM, [5]SN, now at Ruhr University Bochum, [6]Max Planck Fellow Group

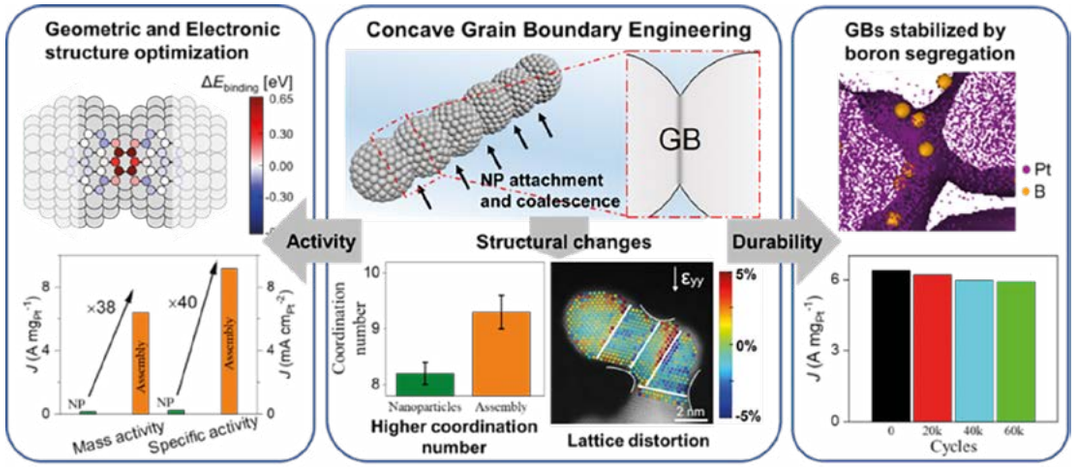

Fig. 1: *By rationally modifying the structure of Pt NP assemblies (middle panel), their geometric and electronic structures can be optimized, resulting in highly active catalysts (left panel). Moreover, a high stability (right panel) can be achieved by doping the high energy interfaces with boron. Figures adapted from our manuscript [2].*

Electrocatalysts increase the rate of electrochemical reactions, making them more rapidly and selectively towards the designed products. As such they are critical to future green technologies, including fuel cells, water electrolyzers, CO_2 electroreduction and the sustainable production of chemicals. As we continue to electrify the society and increase the share of renewable energy to reduce greenhouse gas emissions, the importance of electrocatalysts keeps on growing. However, the most powerful electrocatalysts currently developed are based on scarce and expensive noble metals (e.g., Pt, Pd, Ir, Au), which hinders the widespread use of these technologies.

At the MPI-SusMat, we conduct interdisciplinary research to investigate how the activity, selectivity and durability of current noble metal catalysts can be improved by rationally modifying their nano- and atomic structure and composition. We aim to identify which structural features in materials are beneficial/detrimental to their respective reactions, so that catalysts with an optimized structure and composition can be rationally designed and synthesized.

The complex interplay between structure, chemical composition and catalytic performance requires interdisciplinary expertise. This includes synthesizing the samples, studying their local atomic structure using advanced scanning transmission electron microscopy (STEM) techniques, characterizing their composition in 3D using atom probe tomography (APT) and testing their electrochemical performance as well as durability. Based on these insights we can establish a feedback loop for property optimisation, supported by atomistic simulations and modelling.

One focus in recent years has been to investigate how to improve the performance of widely used Pd nanoparticles (NPs) for the hydrogen-oxidation reaction (HOR) [1] or Pt NPs for the oxygen reduction reaction (ORR) [2]. Both are key electrochemical processes that limit the efficiency of fuel cells and metal-air batteries. Improving performance requires increasing both their mass activity (i.e., activity normalized by mass) and durability. If these two metrics can be simultaneously improved, the catalyst loading on those devices can be reduced, lowering the overall costs.

On Pd catalysts, we showed that the controlled incorporation of B stemming from the solution during wet-chemical synthesis can be used to enhance the activity and stability of NPs [1]. STEM and APT analyses revealed that the Pd forms a network with a ligament thickness of 15 nm with boron embedded within the bulk of the catalysts. Density functional theory (DFT) calculation indicated that the presence of subsurface B lowers the binding energy of H on the Pd(111) surface leading to an increased HOR reaction kinetics. The improved performance was accompanied with an increased durability, proving that our concept of “impurity engineering” provides novel opportunities beneficial for future hydrogen technology developments [1].

In a follow-up study, we synthesized Pt catalyst with a collision process under hydrogen flow [2]. A 38-fold increase in mass activity was achieved by forming Pt NP assemblies (Fig. 1). During the assembly process, randomly oriented Pt NPs attach, re-orient and coalesce, forming concave grain boundary (GB) sites. This increases the average coordination number of the NP assemblies and induces local lattice distortions. As a result, the change in binding energy between the reactant molecules and the surface of the catalytic NPs greatly enhances their catalytic activity. In addition, doping the active GB sites with boron was also proven a successful strategy for maintaining their structural integrity during catalysis. As a consequence, boron-stabilized Pt NP assemblies showed negligible loss (3 %) of ORR activity after 60.000 potential scan cycles (Fig. 1). For comparison, Pt assemblies without boron lost 15 % activity and catalyst consisting of individual Pt NPs lost ~50 % of their initial activity after only 20.000 cycles.

After having seen the potential of GB defects for boosting the catalytic activity of metallic NPs, our next work focused on exploring how the GB density could be controlled, which allowed for a more exhaustive investigation on the relationship between GB and catalytic activity.

Using Au catalyst [3], it was discovered that the GB surface density of the Au NP assemblies could be tailored by changing the frequency of NP attachment and coalescence. Thanks to this discovery, we could synthesize samples with a controlled GB surface density and measure their catalytic performance towards the two-electron ORR. This reaction was chosen because it yields H_2O_2, a product with numerous industrial applications, in a sustainable and clean way, enabling the replacement of the currently used anthraquinone process.

We found a linear relationship between GB surface density and two-electron ORR catalytic activity, highlighting the key role of GBs as promoters of catalytic reactions. The Au NP assemblies with the highest GB density exhibit over a 100 times higher mass activity than the GB-poor Au NPs. The GB-rich NP assembly samples not only performed better compared to GB-poor Au NPs, they also outperformed state-of-the-art two-electron ORR catalysts in acidic media. Boron-doping of Au GBs further enhanced their durability, as negligible activity loss was demonstrated after 100 hours of catalysis. For comparison, without boron doping, the activity of Au NP assemblies dropped by >20 % after 100 hours of the same reaction condition.

In general, our approach, exemplified in Pd [1], Pt [2] and Au [3] NP assemblies, opens a pathway for enhancing the catalytic activity, selectivity and stability of metallic NPs for a wide range of potential reactions.

The work on gold NP assemblies was extended to nanoporous gold (NPG) assembled via thin film dealloying [4]. For its potential as a catalyst, NPG prepared through dealloying of bulk Ag-Au alloys has been extensively investigated. NPG thin films can offer ease of handling, better tunability of the chemistry and microstructure of the nanoporous structure, and represent a more sustainable usage of scarce resources. It is however important to focus on the stability of these films as they are prone to intergranular cracking during dealloying, limiting their potential applications.

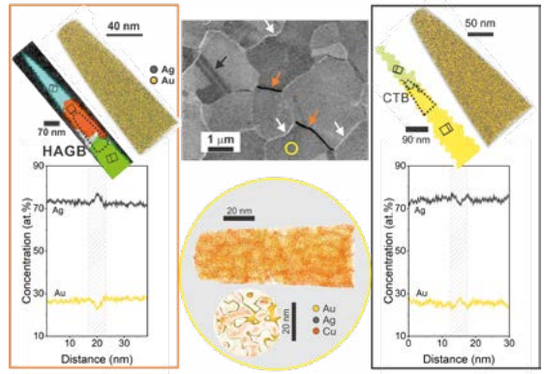

Fig. 2: *The centre image of the dealloyed microstructure showed cracks at HAGBs (orange arrows) and coherency at twin boundaries (black arrow). Chemical segregation at HAGBs (left panel) and twin boundaries (right panel) are systematically investigated to rationalize their stability. Image adapted from our submitted manuscript [4].*

Here, we set out to systematically investigate the local chemistry of grain boundaries in Au-Ag thin films at the subnanometre scale (Fig. 2). Coherent Σ3 grain boundaries appeared more resistant against cracking in comparison to the random high angle grain boundaries (HAGB). This was directly correlated to the pronounced Ag enrichment at the HAGB revealed by APT, whereas Σ3 coherent twin boundaries only showed a mild depletion in Ag. The misorientation and the chemistry of grain boundaries hence affect their dealloying behaviour, which in turn controls the cracking, and the possible longevity of NPG thin films for application in electrocatalysis. The performance and durability of the thin films will be compared to porous Au NP obtained by dealloying of Au-Ag NP [5].

References

1. Kim, S.H., Yoo, S.H.; Shin, S., El-Zoka, A.; Kasian, O.; Lim, J.; Jeong, J.; Scheu, C.; Neugebauer, J.; Lee, H.; Todorova, M.; Gault, B.: Adv. Mater. 34 (2022) 220303.
2. Geng, X.; Vega-Paredes, M.; Lu, X.; Chakraborty, P; Li, Y.; Scheu, C.; Wang, Z.; Gault, B.: Adv. Mater. (2024) 2404839. DOI: 10.1002/adma.202404839.
3. Geng, X.; Vega-Paredes, M.; Ophus, C.; Lu, P.; Ma Y.; Zhang, S.; Scheu, C.; Liebscher, C.; Gault, B.: Nat. Commun. 15 (2024) 8534.
4. Saksena, A; El-Zoka, A.; Saxena, A.; Hatipoglu, E.; Schneider, J., Gault, B.: arXiv:2312.12235.
5. Rurainsky, C.; Nettler, D.R.; Pahl, T.; Just, A.; Cignoni, P.; Kanokkanchana, K.; Tschulik, K.: Electrochim. Acta 426 (2022) 140807.

Tuning nanostructures in thermoelectric materials and developing structure-property relationships

S. Zhang[1], R. Bueno-Villoro[1], L. Gomell[2], H. Bishara[3], C. Jung[1], T. Luo[2], B. Gault[2], C. Scheu[1]

[1]NG, [2]MA, [3]Max Planck Partner Group

Thermoelectric materials convert thermal energy to electrical energy, and vice versa. Such energy conversion can widely contribute to our sustainable future, from cooling applications in modern microelectronics supporting internet-of-things, to renewable power generation from waste heat from industrial activities. Proliferation of these technologies hinges on developing materials with highly efficient thermoelectric energy conversion. Among many materials properties to optimize, efficient thermoelectric materials are required to have low thermal conductivity (κ) and high electrical power factor (σS^2, σ the electrical conductivity, S the Seebeck coefficient) at the same time. Moreover, for their widespread use, it is important to select materials that are abundant in the earth crust.

At MPI-SusMat, we develop a promising class of thermoelectric materials based on semiconducting Heusler (chemical formula: XY_2Z) and half-Heusler (XYZ) phases. The wide choices of X, Y, Z elements enable the selection towards high materials properties and earth abundance. In this report, we will introduce our works on the Heusler VFe_2Al compound [1,2], as well as half-Heusler TiCoSb [3] and NbFeSb [4,5] compounds.

Heusler and half-Heusler materials are well known for their excellent power factor (σS^2), but their thermal conductivity κ is very high compared to efficient thermoelectric materials. Fortunately, κ can be lowered by defect/microstructure engineering, a powerful tool in materials science.

In our research on VFe_2Al, the microstructure was modified by laser surface remelting, a technique from the big family of additive manufacturing. As shown in the misorientation maps in Fig. 1a, the grain structure is significantly refined in the melt pool area, introducing plenty of low angle grain boundaries. Electron channelling contrast imaging (ECCI) further reveals networks of dislocations within the melt pool, as they constitute the low angle grain boundaries (Fig. 1b). As shown in Fig. 1c, chemical segregation around dislocations were analysed by atom probe tomography (APT), where N segregation was found along with depletion in Al.

To understand the roles of increased dislocation density within the melt pool to their functional properties, local electrical and thermal conductivity, σ and κ, were measured by 4-point-probe technique and scanning near-field thermal microscopy, respectively [1]. As shown in Fig. 1d, from outside the melt pool (negative position) to the boundary (0 µm) and inside (positive position), κ shows a monotonous decrease. On the other hand, the electrical transport is not compromised, as electrical resistance $\rho=1/\sigma$ remains similar outside and inside the melt pool, and only increases around the boundary of the melt pool. Overall, the increase in dislocation density by laser surface remelting is proven effective to improve the thermoelectric transport properties. In a follow up study, laser surface remelting was applied in a N_2 atmosphere to stabilize dislocations with N-segregated core at a number density up to 10^{14} m^{-2} [2].

Like dislocations, grain boundaries are also considered effective in impeding heat transfer, and are hence widely applied to reduce κ. Nevertheless, to optimize thermoelectric transport properties, the electrical conductivity σ needs to be maintained high, but grain boundaries are also known to impede transfer of charge carriers. Overall, by decreasing the grain size, there is net gain in thermoelectric conversion efficiency for some materials, and for others, the effect is the opposite.

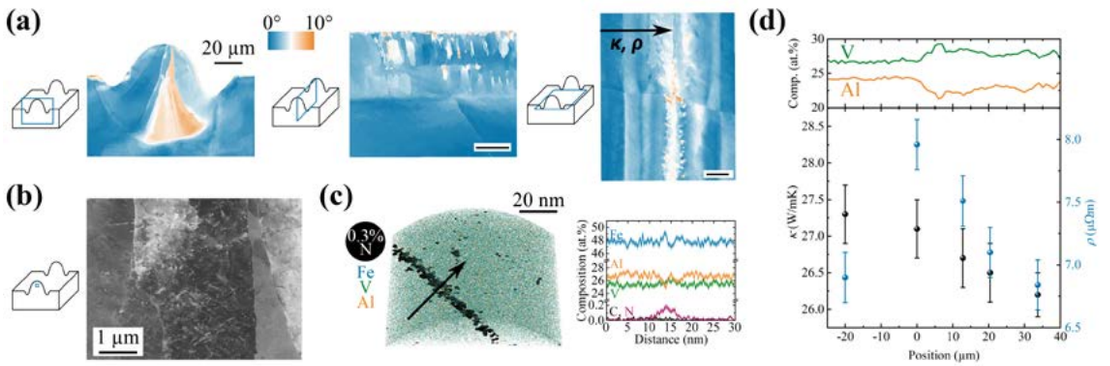

Fig. 1: *(a) Misorientation maps of the grain structures from 3 projections across the melt pool from electron backscattered diffraction. (b) ECCI of the melt pool revealing contrast from dislocations. (c) APT from a melt pool volume showing dislocations enriched in N. (d) Elemental concentration across the line profile (black arrow in (a)), and the local property measurements of κ and ρ=1/σ. Figures are adapted from [1].*

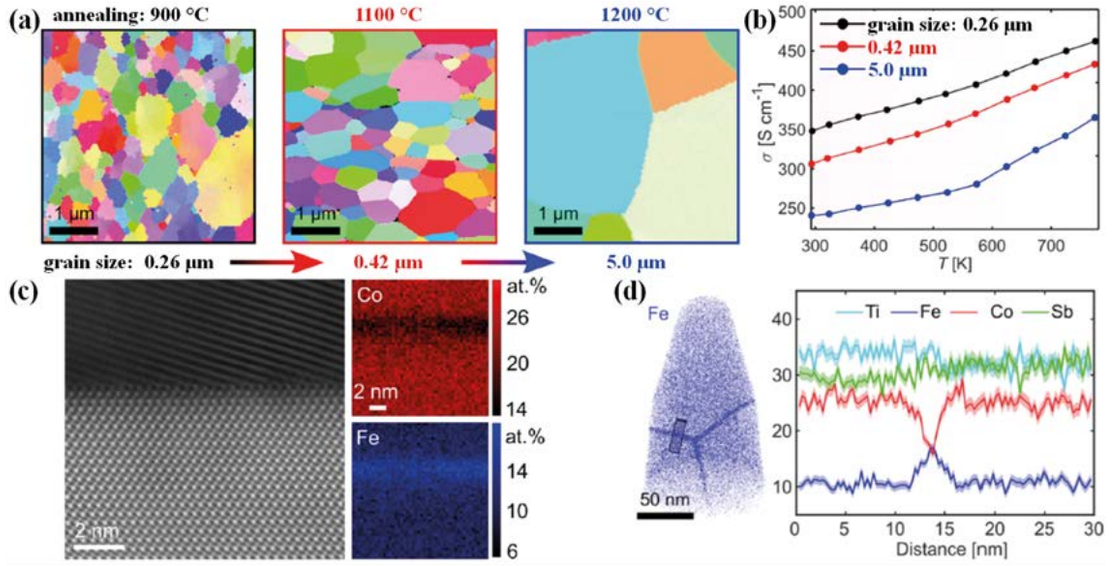

Fig. 2: *(a) The grain size and orientation of $TiCo_{0.7}Fe_{0.3}Sb$ samples annealed at different temperatures. (b) The fine-grain sample shows higher electrical conductivity σ than the coarse-grain samples. (c) Atomic resolution scanning transmission electron micrograph of a $TiCo_{0.7}Fe_{0.3}Sb$ grain boundary with corresponding EDS quantification maps. (d) APT of the fine-grain sample featuring a triple junction and grain boundaries with chemical segregation (line profiles from the cylinder volume). Figures are adapted from [3].*

To understand the effect of grain boundaries in thermoelectric materials, the transport properties of fine-grained and coarse-grained samples are compared. For a fair comparison, the samples were synthesized via the same route of arc melting, ball milling, and sintering processes. The only difference lies in the final step of annealing to promote grain growth. As shown in Fig. 2a, the grain size of $TiCo_{0.7}Fe_{0.3}Sb$ can be tuned over an order of magnitude by varying the annealing temperature, from 0.26 to 5.0 µm.

Most fine-grain materials show lower electrical conductivity σ than their coarse-grain counterparts. As shown in Fig. 2b, it is surprising to observe the opposite trend, as $TiCo_{0.7}Fe_{0.3}Sb$ at 0.26 µm grain size shows the highest σ, while the 5.0 µm grain size sample has the lowest σ. Subsequent observation at the atomic scale reveals elemental redistribution at grain boundaries. As unveiled by energy dispersive X-ray spectroscopy (EDS) (Fig. 2c) and APT (Fig. 2d), a few nanometre region around grain boundaries is enriched in Fe and depleted in Co. Since Fe in $TiCo_{0.7}Fe_{0.3}Sb$ serves as substitutional p-type dopants on Co sites, the enrichment of Fe with corresponding depletion in Co suggests enhanced p-type doping at grain boundaries. As a result, the observed grain boundaries have more charge carriers and lower barriers for their transport than the scenario without chemical segregation, leading to enhancement of σ. As such, we have identified a way to simultaneously increase σ and reduce κ by introducing grain boundaries. In the follow up studies [4,5], we have found new grain boundary phases in NbFeSb materials and understood their effect on thermoelectric transport.

References

1. Gomell, L.; Haeger, T.; Roscher, M.; Bishara, H.; Heiderhoff, R.; Riedl, T.; Scheu, C.; Gault, B.: Acta Mater. 223 (2022) 117501.
2. Gomell, L.; Tsai, S.-P.; Roscher, M.; Bueno-Villoro, R.; Konijnenberg, P.; Zaefferer, S.; Scheu, C.; Gault, B.: Phys. Rev. Mater. 6 (2022) 085405.
3. Bueno-Villoro, R.; Wood, M.; Luo, T.; Bishara, H.; Abdellaoui, L.; Zavanelli, D.; Gault, B.; Snyder, G.J.; Scheu, C.; Zhang, S.: Acta Mater. 249 (2023) 118816.
4. Bueno-Villoro, R.; Zavanelli, D.; Jung, C.; Mattlat, D.A.; Naderloo, R.H.; Perez, N.; Nielsch, K.; Snyder, G.J.; Scheu, C.; He, R.; Zhang, S.: Adv. Energy Mater. 13 (2023) 2204321.
5. Bueno-Villoro, R.; Naderloo, R.H.; Mattlat, D.A.; Jung, C.; Nielsch, K.; Scheu, C.; He, R.; Zhang, S.: Mater. Today Phys. 38 (2023) 101240.

Materials acceleration platforms for sustainable materials

J. Janssen[1], Z. Rao[2], K. N. Sasidhar[2], F. Körmann[1,3], J. Neugebauer[1], D. Raabe[2]

[1]CM, [2]GO, [3]University of Stuttgart

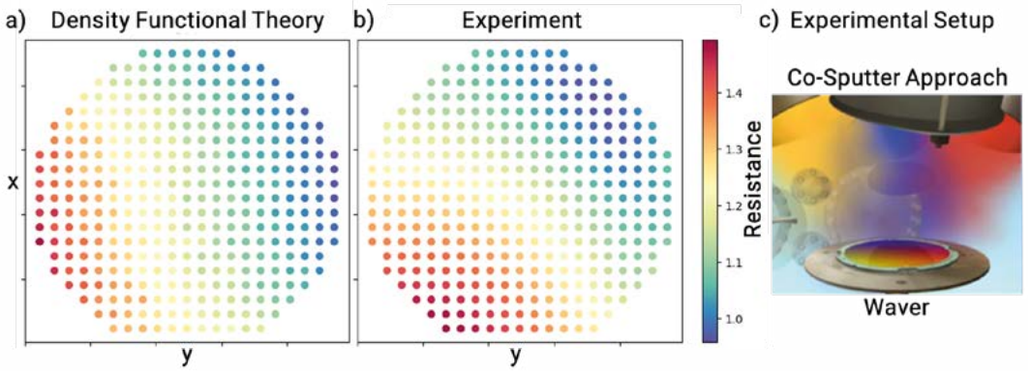

Fig. 1: *Electric resistivity of high entropy alloys calculated with density functional theory simulation (a) in comparison to experimental measurements (b) created by co-sputtering composition spread material libraries (c).*

Given the hierarchical nature of materials, materials science is intrinsically an interdisciplinary research field. This applies especially to the design of sustainable materials, which introduces a series of new constraints. To address these materials science challenges, we combine insights from experiment, theoretical modelling, simulation and more recently data-driven and machine-learned approaches in a materials acceleration platform (MAP). In the following, we highlight three of these MAPs for a range of different materials science challenges:

Electric resistivity analysis of battery materials: In collaboration with partners from the Ruhr University Bochum (RUB) we combine experimental high-throughput synthesis and characterization with density functional theory (DFT) simulations to predict the change in electrical resistivity in relation to the chemical concentration [1]. By creating a digital twin of the composition spread material library (CSML) we identify promising material compositions. The resistivity for the multi-component CSML is predicted using special quasi-random structures (SQS) to approximate the solid solution and the resistivity is calculated as inverse conductivity using the Kubo-Greenwood model for transport properties (Fig. 1a). This approach enables a computationally efficient screening using the pyiron workflow framework (see p. 77). Furthermore, we apply Bayesian optimization to efficiently sample the chemical space and reduce the number of required calculations. The same Bayesian optimization model is afterwards also applied to the experimental measurement (Fig. 1b). By combining the DFT simulation and the experimental measurements in the same Bayesian optimization cycle less than twenty experimental measurements are required to map a five-component CSML. Still, the synthesis of the CSML using co-sputtering remains the most time-consuming process (Fig. 1c), which is not yet integrated in the MAP.

Corrosion resistance: The application of machine-learning for materials design highlights two challenges: on the one hand only positive results are usually published in literature with unsuccessful experiments and simulation remaining hidden but often very important knowledge of the research groups and on the other hand the majority of results are still published with a focus on human-readability rather than machine-readability. One approach to address these challenges is to provide the required research data infrastructure for sharing and publishing experimental and simulation results. To this end, the MPI-SusMat is actively involved in the National Research Data Infrastructure project NFDI Matwerk (see p.86) and is prototyping concepts for the active sharing of research data as part of the Collaborative Research Centre 1394 (see p. 82). These projects are still primarily concerned with future publication and research data. The second direction is the extension of existing machine learning methods to exploit the textual data of existing publications. To bring these new research directions into the design of corrosion-resistant alloys, we have successfully developed two approaches:

In the first approach, a deep neural network (DNN) is extended by word embeddings to include textual data [2]. In this word vectorization approach, each word is tokenized with an integer number. The sentences are then padded with additional zeros, resulting in a constant number of tokens per sentence. As the tokens do not contain any semantic similarity, a word embedding is applied, resulting in a dense vector that is then used as input for the DNN model. The DNN model trained with textual data not only outperforms the reference DNN model without textual data, but also provides the opportunity to use text analysis to identify keywords that influence the prediction.

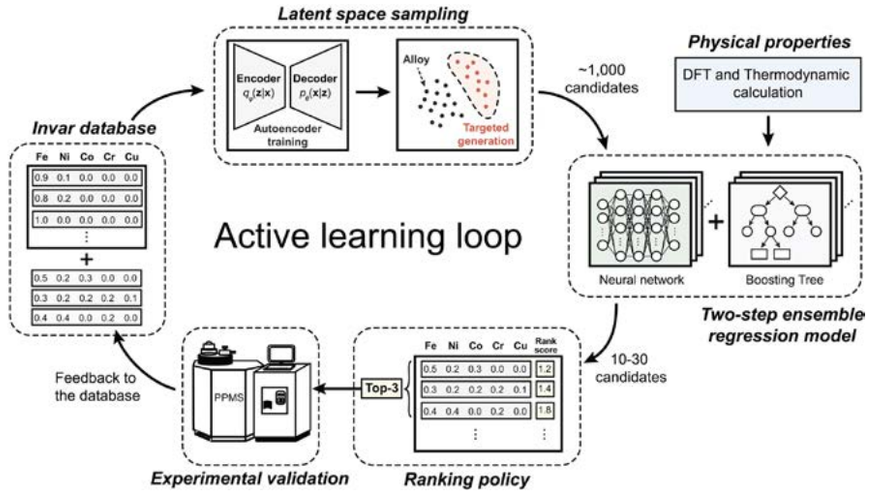

Fig. 2: *Active learning loop combining experiment, simulation and machine-learning to predict Invar alloys with high configurational entropy.*

In the second approach, the input to the DNN model has been extended with additional descriptors based on the alloy composition [2]. This includes the mismatch of atomic radii, configurational entropy, electronegativity, mixing enthalpy, and many more. Adding this chemical understanding of the alloy composition also improves the predictive capability, but not to the same extent as the textual data. The advantage of this chemistry-based approach is its interpretability and resulting extrapolation capability. In terms of corrosion resistance, the positive influence of the presence of Sc and Zr can be predicted, even though neither of these elements were included in the training set.

By combining both, textual data and existing chemical descriptors, the predictive power of current machine learning models to accelerate the discovery of sustainable materials was shown to be dramatically improved.

Data-driven discovery of Invar alloys in high-dimensional chemical configuration spaces: A key advantage of MAPs is that they allow the coupling of experiments, simulation methods and machine learning in a single active learning loop (Fig. 2). This approach has been very successful in navigating the vast chemical configuration space offered by high entropy alloys (HEAs) to discover compositions that optimize target materials properties. A collaboration of the MA and CM department with the MPI-SusMat fellow group of O. Gutfleisch led to the discovery of novel Invar alloys that substantially outperformed conventionally designed HEAs [3]. This was achieved by combining a two-stage ensemble regression model (TERM) with a generative alloy design (GAD) model for high entropy alloys (HEA). The combined model called HEA-GAD-TERM starts with generating alloy compositions using a Wasserstein autoencoder architecture, followed by a screening based on DFT and thermodynamic models to evaluate the empirical Masumoto rule and finally evaluate the predictions experimentally. Such a high throughput screening approach is especially suitable for HEAs given the combinatorial complexity of their chemical space. Finally, the active learning loop is closed with the integration of the casting and experimental measurement of the candidate alloys. This not only validates the predictions of the HEA-GAD-TERM but also improves the predictive capability of the model with every iteration. We find that the cost function for the lowest thermal expansion coefficient is highly non-linear due to the complex underlying composition-property relationships.

The three applications highlight that machine learning, when combined with domain expertise, is a powerful tool for designing sustainable materials. This includes descriptors to provide interpretability of machine learning models. On the other hand, descriptors also allow extrapolation beyond the typically sparse data sets by screening the periodic table. Our machine-learning activities also include the processing of textual data, which still represents the majority of data in materials science. In this direction, the use of Large Language Models (LLM) continues to drive new ideas, such as those of J. Janssen, who won the 2nd LLM Hackathon for 'Applications in Materials and Chemistry'. All these components are combined in the pyiron workflow framework (see p. 77), resulting in a holistic approach coupling experiment, simulation and machine learning.

References

1. Stricker, M.; Banko, L.; Sarazin, N.; Siemer, N.; Neugebauer, J.; Ludwig, A.: arXiv.2212.04804.Sasidhar, K. N.; Siboni, N. H.; Mianroodi, J. R.; Rohwerder, M.; Neugebauer, J.; Raabe, D.: Sci. Adv. 9 (2023) eadg7992.
2. Rao, Z.; Tung, P.-Y.; Xie, R.; Zhang, H.; Ferrari, A.; Klaver, T.P.C.; Körmann, F.; Sukumar, P. T.; Kwiatkowski da Silva, A.; Chen, Y.; Li, Z.; Ponge, D.; Neugebauer, J.; Gutfleisch, O.; Bauer, S.; Raabe, D.: Science 378 (2022) 78.

Machine learning for experiments

A. Saxena[1], Y. Li[2], B. Gault[2], C. Liebscher[3], C. Freysoldt[1]

[1]CM, [2]MA, [3]SN

There are many opportunities to exploit machine learning (ML) in the context of fundamental material science. One might think of, for example, fine-tuning material design for which targets of optimization are clear: the prediction of relevant performance indicators from suitable descriptors of the material's composition and processing can be viewed as a well posed problem for conventional ML models. Once trained, the models can explore the parameter space *in silico* to identify 'hot areas' of optimal performance. However, conventional experiments to measure a specific property are costly. This hinders the immediate application of black-box ML models for novel materials or processing routes, for which little or no prior data is available. Generating input to train data-hungry models, such as neural networks (NN), is typically less efficient than relying on conventional material science theory to rationalize correlations, and thereby lower the complexity of design space. As the dimension of this space increases (by considering more independent variations), a systematic search of all combinations quickly becomes unfeasible. To come up with efficient, goal-oriented experimentation strategies, Bayesian optimization with data-efficient kernel regression may help to balance exploration of unknown corners of parameter space with exploitation of predicted optima.

An alternative route is to focus on techniques that deliver a wealth of data from a single experiment, or from a series of fast experiments on the same sample. Notably imaging experiments (e.g. scanning transmission electron microscopy, STEM), or other spatially resolved materials characterization (e.g. atom probe tomography, APT) provide multi-dimensional data sets that encode both local properties and their variations across the microstructure – exactly those aspects that determine materials' performance and hence are the main targets of optimization. The data challenge, however, is reversed: instead of lacking high-quality data, we must extract relevant patterns from a large amount of possibly noisy raw data.

The main outcome of an APT experiment is a 3D point cloud of the atomic distribution, allowing to determine the composition of a phase or quantify segregation near crystallographic defects. It is rarely clear *a priori* which phases and segregation zones exist, and how to process the atomic positions to quantify composition and geometry in a well-defined, reproducible way. In lack of better options, human scientists use their experience, material-specific assumptions, and visual inspection to define appropriate thresholds.

In order to push toward a more robust analysis, we have developed machine-learning-based tools to extract the composition and geometry of chemical domains in an automated way. The initial step involves segmenting areas with similar chemical compositions by using a multi-stage unsupervised machine learning approach [1]. First, the APT dataset is divided into uniformly sized voxels to gather local compositions, forming a multi-dimensional composition space. Second, in this space, a Gaussian mixture model clusters distinct phases. With this classification of voxels, a density-based clustering algorithm separates different microstructural features of a single phase at voxel resolution. These microstructural entities are then examined for their compositional distribution and geometric character, including orientation, shape, and thickness.

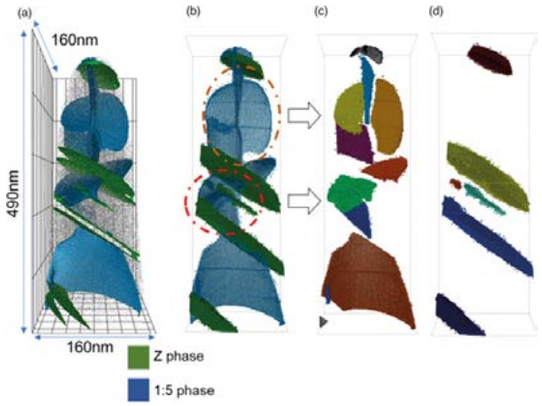

Fig. 1: *APT phase segmentation in a Fe-doped Sm-Co hard magnet. Two precipitate phases (Z phase, 1:5 phase) are identified by composition space clustering (2nd view) in visual agreement with traditional isosurfaces (1st view). Distinct plate-like fragments can be extracted after disentanglement (from [1]).*

For microstructures containing entangled plate-like features, we have developed a workflow using the U-Net model to simplify the segmented microstructural features into individual plates. This allows for systematic measurement of in-plane compositional variations and thickness of each subdomain, as well as their relative orientations (see Fig. 1). The insights gained from analysing these measurements enhanced our understanding of how the second-phase precipitates influence the magnetic properties of Fe-doped Sm-Co alloy, helping guide the design of future permanent hard magnets (see. p. 105).

For segmenting line-like features, particularly dislocations, a computational geometry concept called skeletonization is used. This reduces the iso-composition surface meshes into a linear graph ("skeleton"), encapsulating the topological information of the 3D iso-composition surface mesh. The skeleton is used to segment dislocations for detailed composition analysis. Additionally, crystallographic information from APT data is used for orientation analysis, transforming each dislocation segment into the crystal coordinate system [2]. This workflow successfully extracts and analyses dislocations in a Ni-based alloy, exemplifying its ability to work seamlessly on different APT datasets and its potential to understand the impact of decorated dislocations on material properties.

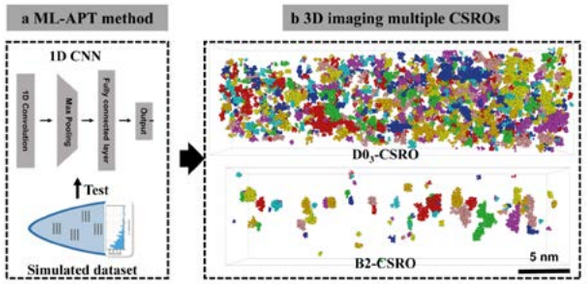

Fig. 2: *3D chemical short-range order (CSRO) imaging in a Fe-18Al alloy. (a) Proposed ML-APT strategy. (b) 3D imaging multiple CSROs. (from [5]).*

Ordering refers to atoms of specific elements self-organizing within an otherwise disordered crystalline matrix. These particular atomic arrangements modify the mechanical and functional properties of materials. Quantitative assessment in three dimensions of the early stage of ordering, what is referred to as short range order (SRO), remains extremely challenging. Since 2021, with support from BiGmax (see p. 83) a series of 1D/2D/3D convolutional neural networks (CNNs) to enhance the analytical capabilities of APT, aiming to go beyond its inherent resolution limits to reveal the size and 3D morphology of multiple chemical long-range and SROs [3,4,5].

These techniques make use of the highest quality, near-atomic depth resolution of APT, combined with its high elemental analytical capability, to generate millions of 1D/2D/3D local structure signatures. The trained CNNs enable the automatic analysis of these signatures without human bias. We showcased our new approach by investigating the origins of the K-state in body-centred-cubic Fe-18Al and Fe-19Ga alloys [5,6]. Fig. 2 summarises how our ML-enabled method works and the complete 3D distribution of domains where ordering is above a certain statistical threshold. Our approach is amenable to investigate chemical short/long-range ordering phenomena in complex metallic materials (see p. 226).

On the side of STEM, our focus lay on further enhancing the extraction of crystalline domains from high-resolution imaging, notably the high-angle annular dark-field (HAADF) channel. In 2021, we had demonstrated that clustering in a space of self-similarity correlations under symmetry operations allowed us to segment distinct grains without prior training of known crystal structures [7]. In collaboration with colleagues from the Fritz Haber Institute, this was now complemented by training a Bayesian NN on simulated data to identify the most common pristine crystal lattices [8]. A Bayesian NN provides the best-matching label, along with an estimate of its confidence, allowing for automatically identifying material defects through the uncertainty distribution in the classification.

A different use of NNs is to use them for coarse-graining. Here, the NN is trained to reproduce the measured data as closely as possible. We have used this to analyse *in situ* phase-transformation monitored by STEM-HAADF. The raw data corresponds to a video, i.e., a noisy, pixelated time series. The NN, on the other hand, represents this data as a continuous function in space and time and thus in a format conforming to continuum models of the transformation. Physics-informed NNs impose additional conditions for the analytic properties. In short, the "loss function" that measures the predictive power of the network is extended by an "equation loss" term that penalizes violations of the underlying partial differential equation. We explored imposing various phase-field models to improve the interpretability of the data and, ideally, extract directly suitable parameters of the phase field model. We found that the NN representation of the measured data is much easier to interpret and amenable to quantification. However, when evaluating the reliability of the parameter extraction for test data from direct phase-field simulations revealed severe limitations. Spatial and temporal gradients, that are linked by the phase-field equations, are high only near the interfaces, which form a very small fraction of the entire data set. In consequence, parameter fitting should focus on these areas, while fitting the overall data ("data loss") must treat all regions equally. Balancing these two requirements is subject to on-going investigations.

References

1. Saxena, A.; Polin, N.; Kusampudi, N.; Katnagallu, S.; Molina-Luna, L.; Gutfleisch, O.; Berkels, B.; Gault, B.; Neugebauer, J.; Freysoldt, C.: Microsc. Microanal. 29 (2023) 1658.
2. Saxena, A.: Machine learning workflows for automatic analysis of atom probe tomography data, Doctoral thesis, RWTH Aachen University (2024).
3. Li, Y.; Zhou, X.; Colnaghi, T.; Wei, Y.; Marek, A.; Li, H.; Bauer, S.; Rampp, M.; Stephenson, L.: npj Comp. Mat. 7, 8 (2021).
4. Rao, Z., Li, Y., Zhang, H., Colnaghi, T., Marek, A., Rampp, M., Gault, B.: Scr. Mater. 234 (2023) 115542.
5. Li, Y., Wei, Y., Wang, Z., Liu, X., Colnaghi, T., Han, L., Rao, Z., Zhou, X., Huber, L., Dsouza, R., Gong, Y., Neugebauer, J., Marek, A., Rampp, M., Bauer, S., Li, H., Baker, I., Stephenson, L.T., Gault, B.: Nat. Commun. 14(2023) 7410.
6. Yan, K., Xu, Y., Niu, J., Wu, Y., Li, Y., Gault, B., Zhao, S., Wang, X., Li, Y., Wang, J., Skokov, K.P., Gutfleisch, O., Wu, H., Jiang, D., He, Y., Jiang, C.: Acta Mater. 264 (2024), 119583.
7. Wang, N.; Freysoldt, C.; Zhang, S.; Liebscher, C. H.; Neugebauer, J.: Microsc. Micronanal. 27 (2021) 1454 .
8. Leitherer, A.; Yeo, B. C.; Liebscher, C. H.; Ghiringhelli, L. M.: npj Comp. Mat. 9 (2023) 179.

Atom probe tomography and field ion microscopy

F. Morgado[1], S. Bhatt[2], S. Katnagallu[1,2], C. Freysoldt[2], B. Gault[1]

[1]MA, [2]CM

Atom probe tomography (APT) has developed into a valuable tool for nano-scale chemical analysis in material science. APT's sensitivity to impurities down to the ppm level combined with its sub-nm spatial resolution provide deep insights into the interplay of chemical composition and microstructural features. However, the complex physics that underpins APT involves phenomena that are not completely understood. In order to push the limits of APT, MPI-SusMat works on improving experimentation (see p. 65), theoretical modelling, and data processing (see p. 68).

Here, we focus on the aspect of correlating the chemical identity with atomic arrangements. In APT, the reconstructed 3D positions are insufficiently precise to derive atomic configurations [1]. Thus, the crystallographic character of defects that lead to segregation is not directly accessible. If, however, the APT experiment is performed in the presence of an imaging gas (e.g. He, Ne), an additional field ion microscopy (FIM) setup is realized – this is the analytical FIM (a-FIM) technique pioneered at the institute in 2019 [2]. An essential task is to separate the signal of continuous field ionization of the imaging gas from the pulse-induced field evaporation events by filtering the detector raw data for correlated events [2,3]. This filtering and the resolution of the a-FIM technique was further refined in the reporting period [4].

One of the remarkable achievements of a-FIM is a direct proof of chemical contrast, i.e., the fact that the (relative) brightness of a spot in FIM can be indicative of the chemical identity. The origin of this contrast lies in the electronic structure, and is hence amenable to simulations with density functional theory (DFT), as demonstrated by preliminary work in the preceding period based on the Tersoff-Hamann approximation to predict tunneling currents from the local density of states above the surface. Jointly, the Freysoldt and Gault groups have used a-FIM to demonstrate segregation of Re to dislocations [2], interactions between vacancies and Ta [4], and finally segregation of W to stacking faults, as summarized in Fig.1. These observations could not be performed by APT, because of limitations in the spatial resolution [1].

The Freysoldt group has then developed a novel simulation framework for local contrast in FIM that showed excellent agreement with experimental findings [5]. In FIM, electrons tunnel from an imaging gas atom into the surface. In presence of a field, however, the electronic states decay rapidly above the surface. Their small absolute magnitude in the region of interest exposes the limited accuracy of existing algorithms, and the computed wavefunctions 5–10 Å above the surface are dominated by noise. To circumvent this issue, we introduced EXTRA (extrapolation of tails via reverse integration algorithm) [5] that works on a local scale and that remains stable over many orders of magnitude (see Fig. 2). The improved accuracy allowed us to drop *ad hoc* assumptions on where ionization takes place in space and energy. Our results for Ni show that the empty d-orbitals of Ta, W, Re are responsible for the contrast, even if they do not lie directly above the Fermi level. These results suggest that different species can be discriminated based on their relative intensity. We will exploit these theoretical insights in

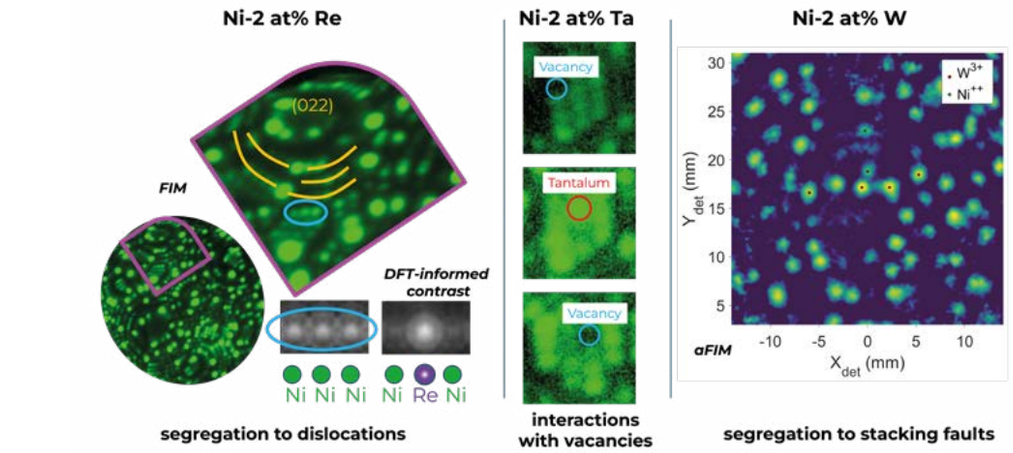

Fig. 1: *FIM and aFIM for three binary Ni-alloys showcasing the possibilities for imaging interactions of solutes and crystal defects (images from Ref. [2, 4] and unpublished).*

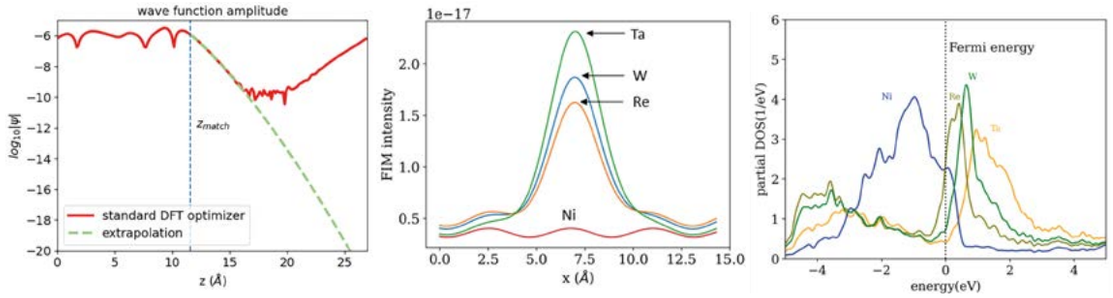

Fig. 2: *Simulations of FIM contrast. (a) EXTRA wave function extrapolation overcomes accuracy limitations in the vacuum region. (b) Simulated FIM intensity profiles for various impurities in Ni. (c) The origin of contrast: impurities provide more states above the Fermi level.*

combination with improved experimental protocols in a newly established Collaborative Research Centre to elucidate the surface atomic arrangements of high-entropy alloys for electrocatalysis(see p. 90).

An open question is to what degree the atomic arrangement seen in FIM is intrinsic to the sample, or the result of the high-field conditions in experiments. We simulated field evaporation and electrified surfaces in density-functional theory to investigate the formation of vacancies [7]. For Pt and Ni as prototypical fcc metals, we find that the formation of vacancies at surfaces with kinks becomes less favourable upon applying a voltage. Below the surface, the Maxwell stress modifies defect stability according to the defect's excess volume. Directly at the surface, the field energy in the empty space of a newly formed vacancy adds to its formation energy. We further showed that the field alters the migration barriers. Vacancy outward diffusion implies the inward diffusion of a surface atom, and this inward motion shows qualitatively the same field effect as the field evaporation – except that the direction is reversed: the barriers get larger compared to the field-free surface. This is even more pronounced for positively charged impurities.

Another crucial aspect of atomic arrangements under the influence of an electric field is the field evaporation path taken by the evaporating ion. Our recent simulations indicate that field evaporation is a competing process between field-induced desorption and field-induced surface diffusion. By using the electric field as a variable to construct a surface phase diagram for Li, we can explain the inhomogeneous field evaporation of Li observed experimentally. Our calculations demonstrate that Li undergoes exothermic dissolution of kink atoms at high electric fields, but below the critical field evaporation strength. This destroys the atomic configuration of Li. Additionally, the electric field significantly reduces surface diffusion barriers and changes the preferred adsorption sites from on top to bridge sites. This shift is attributed to the strong dimer-like bond formation between the Li adatom and surface atom, along with their relative stabilities under the electric field.

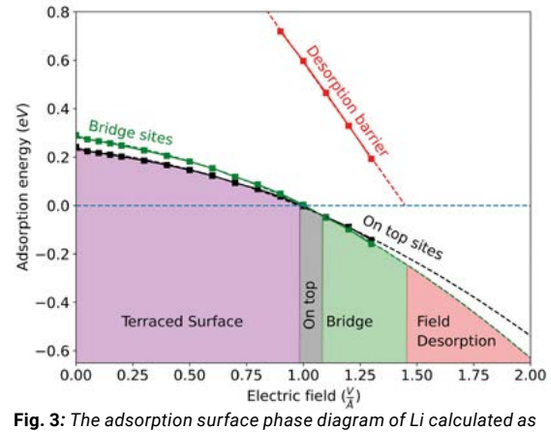

Fig. 3: *The adsorption surface phase diagram of Li calculated as a function of electric field. The adsorption energies for the on top and bridge sites are plotted as a function of electric field. And the field desorption barrier (for on top) as a function of field is also plotted.*

References

1. Gault, B; Klaes, B.; Morgado, F. F.; Freysoldt, C.; Li, Y.; De Geuser, F; Stephenson, L. T.; Vurpillot, F.: Microsc. Microanal. 28 (2022) 1116.
2. Katnagallu, S. S.; Stephenson, L. T.; Mouton, I.; Freysoldt, C.; Subramanyam, A. P. A.; Jenke, J.; Ladines, A. N. C.; Neumeier, S.; Hammerschmidt, T.; Drautz, R.; Neugebauer, J.; Vurpillot, F.; Raabe, D.; Gault, B: New J. Phys. 21 (2019) 123020.
3. Katnagallu , S.S., Morgado, F.F., Mouton, I., Gault, B., Stephenson, L.T.: Microsc. Microanal. 28 (2022) 1264.
4. Morgado, F. F.; Stephenson, L.; Rousseau, L.; Vurpillot, F.; Evertz,S.; Schneider, J. M.; Gault, B: Microsc. Microanal. 29 (2023) 1077.
5. Bhatt, S.; Katnagallu, S.; Neugebauer, J.; Freysoldt, C.: Phys. Rev. B 107 (2023) 235413 .
6. Morgado, F. F.; Katnagallu, S.; Freysoldt, C.; Klaes, B.; Vurpillot, F.; Neugebauer, J.; Raabe, D.; Neumeier, S.; Gault, B.; Stephenson, L.: Scr. Mater. 203 (2021) 114036.
7. Katnagallu, S.; Freysoldt, C.; Gault, B.; Neugebauer, J.: Phys. Rev. B 107 (2023) L041406.

Automated machine learning approaches for *ab initio* thermodynamics

M. Poul[1], S. Menon[1], R. Dsouza[1], L.-F. Zhu[1,2], B. Bienvenu[1], J. Janssen[1], T. Hickel[1,3], J. Neugebauer[1]

[1]CM, [2]University of Stuttgart, [3]Bundesanstalt für Materialforschung und -prüfung (BAM)

The *ab initio* prediction of material properties under realistic conditions is a long-standing goal of computational materials science. In this context, the CM department is well known for the thermodynamic integration using Langevin dynamics (TILD) methods, which achieve not only qualitative but also quantitative agreement with experimental measurements for thermodynamic properties such as the heat capacity of unaries. These methodologies have been successfully extended to study the temperature as well as concentration dependent phase stability. This allows us the prediction of phase diagrams with *ab initio* accuracy like the one in Fig. 1 (a-c) [1]. These can be directly compared to CALPHAD phase diagrams, which are mainly based on experimental data (Fig. 1 d). While the quantitative agreement remains challenging due to the limits of the underlying density functional theory (DFT) calculations, the current results already highlight the impact of machine learned interatomic potentials (MLIP). When fitted to a training set that covers the relevant regions of the phase space, they provide sufficient flexibility to capture the phase stability (Fig. 1 b,c) in contrast to previous approaches such as the embedded atom model (EAM) potential (Fig. 1 a). Like the EAM potential, the MLIP approximates the energy and forces of a single atom based on its local environment, enabling linear scaling with the number of atoms. However, with several thousand rather than a few tenths of parameters and local atomic descriptors based on the atomic cluster expansion (ACE), they can be fitted to reproduce the accuracy of *ab initio* energies such as DFT with a root mean square error (RMSE) of ~1meV. To make these approaches accessible to a broad community, the automation of complex DFT calculations, ML potential fitting and phase diagram construction is crucial. To achieve this, the following three challenges had to be addressed:

Diverse training sets: The predictive power of any machine learning model is limited by its training set. Machine learning models are very effective for interpolation but perform poorly on extrapolation, and MLIPs are no different. To achieve high precision over the entire temperature and concentration range, M. Poul has developed the Automated Small Symmetric Structures Training (ASSYST) approach [2]. Starting from the high-symmetry structures of the different space groups, the approach generates a diverse training set of structures, by displacing individual atoms and relaxing the resulting structures. The space-group symmetry combined with relaxations, faithfully samples the physically relevant part of phase space. In addition, the atomistic structures are relatively small with ~10 atoms, so they can be evaluated computationally efficiently with DFT. The potentials trained on this diverse training set can describe relevant bulk phases, complex defects and even the bulk phase diagrams without requiring explicit fitting to relevant atomic structures. Thus, without the need to continuously expand the training set in an active learning loop, the ASSYST approach directly provides a diverse training set in one step. Being independent of the MLIP architecture, ASSYST-generated structures provide a systematic approach to generate training sets for studying phase diagrams like Fig. 1, as well as benchmarks for comparing different MLIP architectures [1].

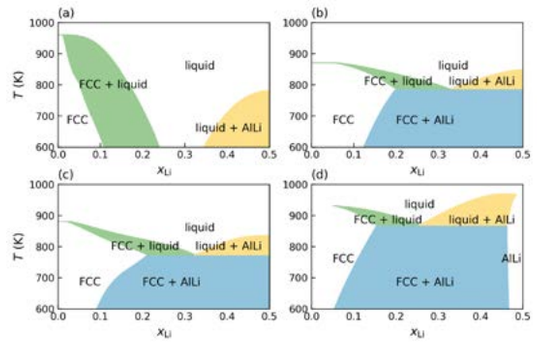

Fig. 1: *Aluminium-Lithium phase diagram calculated using (a) a classical embedded atom model potential, (b) a neural network potential and (c) an atomic cluster expansion potential in comparison to the (d) CALPHAD reference.*

Physical properties: The local descriptors of the MLIPs are based only on the coordinates of the atoms so they do not include any information about physical properties such as charge or magnetic moments. Without the inclusion of the magnetic moments in the MLIP, a wide range of material systems, including for instance iron and its oxides, cannot be simulated, resulting in unphysical predictions. To construct an MLIP for a magnetic material, like iron or its oxides, the structure set generation is extended by including the sampling of the magnetic degrees of freedom. This is achieved by exploring different collinear magnetic configurations on the Fe sub-lattice, i.e. considering the same structure with different orientations of the spins. The resulting structure set is fitted with an ACE potential. B. Bienvenu extended the atomic cluster expansion (ACE) potential to include the magnetic degrees of freedom using an Ising-like description [3]. The potential is fitted considering three types of Fe atoms defined according to the sign of their spins: spin up, spin down and non-magnetic, without considering the magnitude. With this computationally efficient and effective approximation of magnetism large-scale simulations can be performed at a reasonable computational cost. At the same time the approach drastically cuts the number of configurations required to sample the non-collinear magnetic degrees of freedom. Finally, by dynamically evolving both the atomic positions and the magnetic moments in a molecular-dynamics simulation with on-the-fly Monte Carlo swaps between the different magnetic species (spin up, down and non-magnetic), we were able to include the magnetic contributions in our adiabatic approach to compute the free energy. Compared to an MLIP potential without the explicit inclusion of magnetic moments, we achieve a higher level of precision when fitting the training dataset with different magnetic configurations. Even more importantly, we reproduce the physically correct magnetic orders and thermodynamics of the Fe-O binary system in comparison to experiment. This again highlights the effectiveness and data efficiency of this Ising-like description of the magnetic moments.

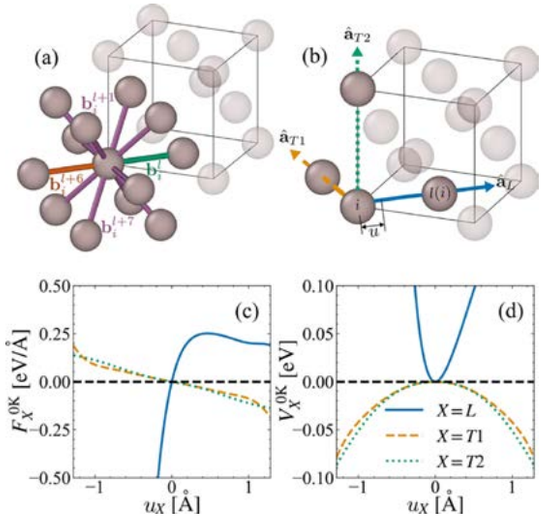

Fig. 2: *The anharmonic mean-field bond model constructed from (a) the symmetries and correlations of nearest-neighbour bonds. (b) Large displacements of an atom result in a locally anharmonic (c) force and (d) potential, which are used in the model.*

Efficient sampling: On the one hand, the high precision of the MLIPs compared to previous EAM potentials allows to replace the costly thermodynamic integration in the TILD approach by more efficient free energy perturbation calculations, while maintaining *ab initio* accuracy in the sub-meV range. This approach, developed by L.-F. Zhu allows easy extension from unary and binary [4] to multi-component materials and has been successfully applied to the study of high entropy alloys [5]. On the other hand, there is a continuous effort to develop strategies to eliminate the need for thermodynamic sampling itself by using analytical models. R. Dsouza derived an improved mean-field anharmonic bond (MAB) model [5, 6], which calculates explicit anharmonic free energies using bond densities constructed using the mean-field theory. The densities are constructed from the anharmonic pair-potential and the application of bond symmetries and bond pair correlations, as illustrated in Fig. 2. By constraining appropriate thermodynamic variables such as temperature, pressure, and volume, the model predicts properties such as free energy, heat capacity, and thermal expansion. This sampling-free estimation is an improvement over the commonly used quasi-harmonic approximation in terms of numerical accuracy and is many orders of magnitude more computationally efficient than thermodynamic integration methods.

All of these recent methodological developments are implemented in the pyiron workflow framework (see p. 77), enabling the calculation of phase diagrams with *ab initio* accuracy, as highlighted in Fig. 1. This not only demonstrates the collaboration within the CM department addressing this challenge as a team, but also beyond the department. S. Menon coordinated this collaboration with partners from the Ruhr University Bochum and the Technical University Darmstadt (see p. 97), who applied the same workflow for different types of interatomic potentials to assess their ability to span the whole phase space required for the phase diagram [1]. While the quantitative agreement with experimental phase diagrams remains challenging and the individual steps still require specialized expertise, a major step towards the automated calculation of *ab initio* phase diagrams has been taken. From this perspective, having all the steps from the construction of the training data set, over the DFT calculations and the fitting of the MLIP up to the calculation of the free energies and the construction of the phase diagram, in a single pyiron workflow is not only a technical achievement, but also highlights the understanding of the underlying physics. It is now possible to replace existing methodologies like building blocks with new ones and to benchmark the new methodologies by direct comparison to the experimental phase diagram, enabling routine calculations of *ab initio* phase diagrams and *ab initio* materials design studies. The same applies to computationally highly efficient models, such as the recently developed MAB model, which can be directly benchmarked to quantify their impact on accelerating the calculation of *ab initio* phase diagrams.

References

1. Menon, S.; Lysogorskiy, Y.; Knoll A.L.M.; Leimeroth, N.; Poul M.; Qamar M.; Janssen, J.; Mrovec, M.; Rohrer, J.; Albe, K.; Behler, J.; Drautz, R.; Neugebauer, J.: arXiv:2403.05724.
2. Poul, M.; Huber, L.; Bitzek, E.; Neugebauer, J.: Phys. Rev. B 107 (2023) 104103.
3. Bienvenu, B.; Todorova M.; Neugebauer, J; Mrovec M.; Lysogorskiy, Y.; Drautz R.: arXiv:2407.13903.
4. Zhu, L.-F.; Srinivasan, P.; Gong, Y. L.; Hickel T.; Grabowski B.; Körmann F.; Neugebauer J.: Phys. Rev. B 109 (2024) 094110.
5. Zhu, L.-F.; Körmann, F.; Chen, Q.; Selleby M.; Neugebauer, J.; Grabowski, B.: arXiv:2408.08654.
6. Dsouza, R.; Huber, L.; Grabowski, B.; Neugebauer, J; Phys. Rev. B 105 (2022) 184111.
7. Dsouza, R.; Poul, M.; Huber, L.; Swinburne T.D.; Neugebauer, J.; Phys. Rev. B 109 (2024) 064108 .

StahlDigital: Digital workflows for the steel industry

F. Roters[1], B. Liu[1], T. Jogi[1], U. Saiki[2], T. Hickel[2]

[1]MA, [2]CM

StahlDigital was a project funded by the Federal Ministry of Education and Research running from 2021 to 2024, where MPI-SusMat studied a typical process chain for the production and processing of semi-finished steel products and the use of components as shown in Fig. 1 together with two academic partners.

The aim of StahlDigital was to develop an interoperable ontology-based workflow with associated data storage (following the FAIR principles [1]) in a modular data space and to demonstrate the added value for e.g. the use case of car body components and to integrate the results into the MaterialDigital (see p. 88) platform.

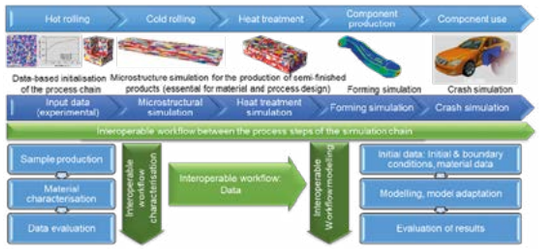

Fig. 1: *Illustration of a typical process chain in steel processing and corresponding multiscale process chain simulation and materials characterization workflows.*

To achieve this goal, first a steel ontology had to be developed. For this task the partner InfAI (Leipzig) developed an ontology-pipeline that allows the creation of an ontology based on a simple Excel spread sheet filled with a vocabulary based on the knowledge of the domain experts. Second, a Dataspace Management System (DSMS) to collect, store, and retrieve data was set up by the partner Fraunhofer IWM (Freiburg). The main task of MPI-SusMat was the development of workflows along the process chain and along different length scales (Fig. 1) based on the workflow management system pyiron (see p. 77).

Here, we first present a proof-of-concept example for coupling different length scales, before two examples for steel related process workflows using the workflow management tool pyiron that have been developed and improved within project StahlDigital are presented. Finally, the extension of pyiron for a semantic description of workflows is presented.

Combination of LAMMPS and DAMASK

As a proof of concept, we constructed a pyiron workflow, combining a special quasi-random structures (SQS) generation tool [2], an atomistic simulation tool (Lammps), and a continuum simulation tool (DAMASK, see p. 78, [3]) to perform numerical homogenization of single crystal properties of iron with different additions of aluminium. While the elastic constants of the pure materials are readily available in the literature, this is not true for the alloys. Using interatomic potentials available for the Fe-Al system, molecular dynamics simulations are performed with Lammps to determine the single crystal elastic constants. These are then passed into DAMASK, which is used to probe the stress-strain behaviour of a polycrystal for three different Al concentrations (Fig. 2). The workflow needs to run a huge number of individual simulation jobs. In this case, pyiron takes full care of distributing the individual jobs to computing nodes, collecting the results, and at the same time recording important metadata about the jobs in a SQL database.

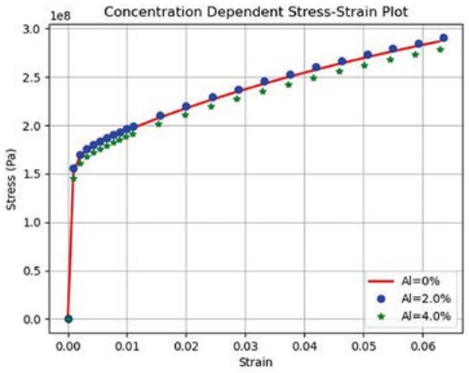

Fig. 2: *Effect of the single crystal elastic constants of Fe-Al solid solutions with three different Al concentrations on the macroscopic stress-strain response. Plasticity parameters were intentionally kept constant.*

Rolling simulation with DAMASK

The pyiron continuum module has been extended to facilitate the simulation of a multi-stand rolling process. The class ROLLING allows to define a single rolling step by specifying the height reduction and the rolling speed. The actual simulation is based on DAMASK RVEs (Representative Volume Element). The rolling deformation is approximated as plane strain compression and the respective DAMASK load file is automatically created. As the total deformation during multi step rolling can become very high, it can be specified for each rolling step whether a regular grid should be restored, so-called regridding, before applying the next rolling step. In this way any number of rolling steps can be simulated. Fig. 3 shows the example of a four-step rolling process. For illustration purposes regridding is applied before rolling steps 2 and 4, even though not necessary from a numerical point of view.

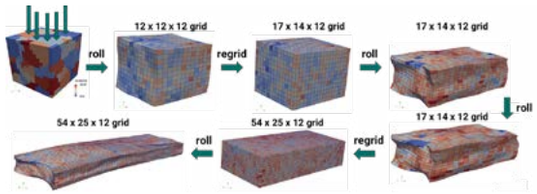

Fig. 3: *Simulation of a 4-stand rolling process. The colours indicate the height reduction (blue low, red high).*

Heat treatment with OpenPhase

The simulation of a final heat treatment to recrystallize the rolled microstructure is simulated using OpenPhase (academic) [4]. As OpenPhase works with regular grids only, the first step is a regridding of the final deformed microstructure obtained from the rolling simulation (Fig. 4, top left). Next the OpenPhase configuration is created and a specified number of nuclei is placed in the areas with highest deformation. As the phase-field method uses diffuse interfaces the grain boundaries are smoothed as a final pre-processing step (Fig. 4, top right). Finally, during the actual OpenPhase simulation these nuclei grow on the cost of the deformed grains (Fig. 4, bottom).

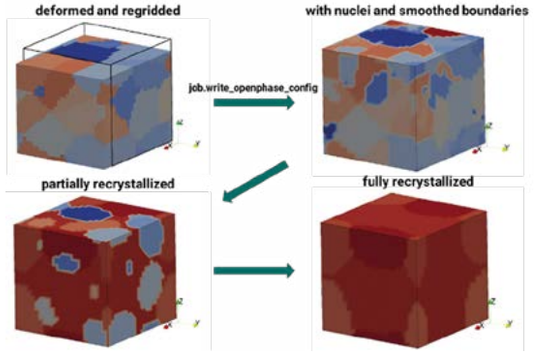

Fig. 4: *Simulation of recrystallization during heat treatment. The colours only serve to visualize the grains and have no special meaning.*

Semantic description of workflows

The coupling between different simulation/experimental tools required for the steel development process, as shown in Fig. 1, is generally achieved by converting output of one tool to serve as input for another tool. Using ontology-based concepts we can overcome such direct coupling between different tools. The idea is to use ontologies as an abstraction layer to define relations between data and concepts, which can be exploited for workflows and program interfaces (Fig. 5). Such abstraction allows a flexible exchange of different tools that serve the same purpose within a workflow. In this way workflows can be defined independently of the underlying simulation/experimental tools.

Towards achieving this goal, we have adopted two different levels of ontology-based approach in pyiron: (i) Extract metadata from pyiron simulation and derive ontology relations using the pyiron class hierarchy. (ii) Automatic generation of ontology-based workflows.

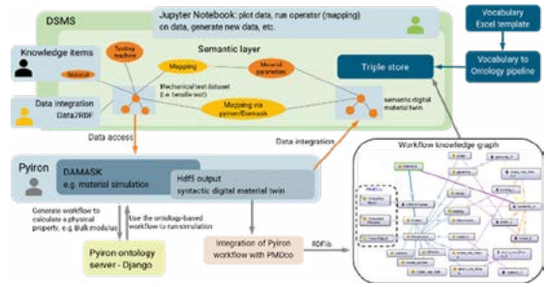

Fig. 5: *Combining syntactic and semantic workflow descriptions using the developed StahlDigital ontology, pyiron, and the StahlDigital dataspace powered by DSMS.*

For the first approach, we create a metadata table for the pyiron simulation environment with different sections on (i) codes, (ii) the input and output parameters, (iii) the reference jobs and (iv) the physical units. The metadata table is then mapped to the Platform Material Digital Core Ontology (PMDco) in class and subclass relationships using RDFlib, where we add codes to the PMDco class SimulationProcess and Parameters to ValueObject. The simulation data from the hdf5 file of the finished pyiron workflow is extracted by running a PyironTable job. We compare the pyiron job input/output with metadata information and map those data in the application ontology that are defined in the metadata table. We afterwards follow the PMDco guidelines to derive correct classes, object property, and data property relations.

In the second approach, an owl database for pyiron is created, which contains the information about necessary data-property relations, and is accessible from a Django-pyiron ontology server as shown in Fig. 5. Based on the required output physical quantity, an ontology-based pyiron workflow is generated. Using pyiron, this workflow can be executed in a fully automated manner, which returns the value of the required physical quantity as an output.

References

1. Scheffler, M.; Aeschlimann, M.; Albrecht, M.; Bereau, T.; Bungartz, H.-J.; Felser, C.; Greiner, M.; Groß, A.; Koch, C. T.; Kremer, K.; Nagel, W. E.; Scheidgen, M.; Wöll, C.; Draxl,V: Nature 604 (2022) 635.
2. dgehringer, sqsgen, https://github.com/dgehringer/sqsgenerator, accessed: June, 2024.
3. Roters, F.; Diehl, M.; Shanthraj, P.; Eisenlohr, P.; Reuber, C.; Wong, S.L.; Maiti, T.; Ebrahimi, A.; Hochrainer, T.; Fabritius, H.-O.; Nikolov, S.; Friák, M.; Fujitai, N.; Grilli, N.; Janssens, K.G.F.; Jia, N.; Kok, P.J.J.; Ma, D.; Meier, F.; Werner, E.; Stricker, M.; Weygand, D.; Raabe, D.: Comput. Mater. Sci. 158 (2019) 420.
4. ICAMS, OpenPhase academic, https://openphase.rub.de, accessed: June, 2024.